André Espírito Santo Pedrosa

EXPLORING TISSUE CHARACTERIZATION BY TEMPERATURE INDUCED CHANGES ON ULTRASOUND BACKSCATTERED ENERGY

Thesis submitted to the University of Coimbra in compliance with the requisites for the degree of Master in Biomedical Engineering

September, 2016

· U C ·

Universidade de Coimbra

• U C •

FCTUC FACULDADE DE CIÊNCIAS
E TECNOLOGIA
UNIVERSIDADE DE COIMBRA

André Espírito Santo Pedrosa

Exploring tissue characterization by temperature induced changes on ultrasound backscattered energy

Thesis submitted to the

University of Coimbra for the degree of

Master in Biomedical Engineering

Supervisor:

Prof. Doutor César Teixeira (University of Coimbra)

Jury:

Prof. Doutor César Teixeira (University of Coimbra)

Prof. Doutor Jaime Santos (University of Coimbra)

Prof. Doutor Pedro Martins (University of Coimbra)

Coimbra, 2016

This work was developped in collaboration with:

Centro de Informação e Sistemas da Universidade de Coimbra

Laboratório de Ultrassom, Programa de Engenharia Biomédica,
COPPE - Universidade Federal do Rio de Janeiro

Acknowledgments

I would like to express my appreciation to Prof. Doutor César Teixeira for his guide, orientation and constant availability along this thesis. Also a word to the researchers of Laboratório de Ultrassons do Programa de Engenharia Biomédica do COPPE-Universidade Federal do Rio de Janeiro, especially to Prof. Doutor Wagner Coelho and Prof. Doutor Marco António von Krüger, for providing me with technical knowledges in a real experimental laboratory. I also would like to thank Eng. Ricardo Simões for his help, attention and companionship from the beginning and through out this work. Finally, I would like to thank my colleagues and friends for the experiences, moments and help. To my parents, Emídio and Madalena, and for my sister Tatiana as well, a sincerely word of gratitude for the support, encouragement, and patience along this years.

The authors acknowledge the financial support of the Luso-Brazilian cooperation project CAPES/FCT Thermo - response " (FCT/CAPES: 10172/13-0), CNPq and FAPERJ, that enabled the development of the computational simulation part of this thesis at the University of Coimbra, and the experimental part at the Laboratório de Ultrassom of the COPPE-Universidade Federal do Rio de Janeiro.

Acknowledgements also to the Laboratory for Advanced Computing at University of Coimbra (URL http://www.lca.uc.pt) for providing HPC, computing, consulting resources that have contributed to the research results reported within this paper.

Financing

This work had the financial support from the Luso-Brazilian cooperation project CAPES/FCT *" Thermo - response "* (FCT/CAPES: 10172/13-0) and from CNPq and FAPERJ, that enabled the development of the computational simulation part of this thesis at the University of Coimbra, and the experimental part at the Laboratório de Ultrassom of the COPPE-Universidade Federal do Rio de Janeiro.

“ When Thomas Edison worked late into the night on the electric light, he had to do it by gas lamp or candle. I’m sure it made the work seem that much more urgent.”

George Carlin

Resumo

A ultrassonografia é uma técnica de imagiologia médica vastamente utilizada devido ao facto de ser não-invasiva, relativamente barata, versátil e permitir a aquisição de imagens em tempo real. No entanto apresenta algumas desvantagens, tais como a moderada resolução e o baixo contraste que diminuem bastante a qualidade das suas imagens, comparando com técnicas como a ressonância magnética e a tomografia computorizada. Este facto levou a que, nos últimos anos, tenham surgido diversas metodologias no sentido de conferir às imagens ultrassonográficas tradicionais melhor qualidade e quantidade de informação. Exemplo disso são os casos da elastografia e do Doppler Color Flow Imaging que fornecem informação acerca da rigidez dos tecidos e dos fluxos sanguíneos, respetivamente.

A literatura reporta mudanças monótonas da energia retro espalhada (Changes in Backscattered energy - CBE) quando a temperatura do meio é aumentada. Estas alterações são características do tipo de espalhador presentes no meio: meios compostos por espalhadores típicos de tecidos musculares dão origem a curvas de energia retro espalhada decrescentes com o aumento da temperatura, ao contrário de meios compostos por espalhadores típicos de tecidos adiposos que apresentam o comportamento inverso. Estas propriedades foram anteriormente estudadas com o objetivo de mapear a temperatura durante terapia por ultrassons.

Este trabalho tem por objetivo o estudo de uma metodologia que visa a caracterização não invasiva de tecidos para potencialmente dotar imagens convencionais de informação adicional sobre o meio em análise. A nova metodologia é baseada em mudanças na energia retro espalhada que se manifestam em variações de intensidade nas imagens ultrassónicas convencionais quando o meio irradiado é aquecido. Foi possível usando sinais e imagens de ultrasons, simuladas com a toolbox para o Matlab denominada k-Wave, desenvolver a nova metodologia cujos resultados são coerentes com os modelos teóricos presentes nos estudos de *Straube* e *Arthur* que de-

screvem a energia retro espalhada esperada para um determinado volume de tecido. Usando dados adquiridos com amostras *ex-vivo* de músculo e gordura suína, foi possível obter curvas de CBE distintas para cada uma delas. Esta nova técnica poderia por exemplo ser o ponto de partida para um método simples e barato para classificar tecidos não invasivamente.

Abstract

Ultrasounds are widely used in medical imaging due to the fact of being non-invasive, relatively cheap, flexible and to allow real-time acquisitions. However it has some disadvantages, such as the moderate resolution and the low image contrast that greatly limits the image quality comparing to techniques as magnetic resonance or computed tomography. This lead, in the last years, to the development of multiple methodologies in an effort to provide traditional ultrasound images with better quality and amount of information. Example are the cases of elastography and Doppler Color Flow Imaging that provide information about tissues rigidity and the blood flow, respectively.

Literature reports monotonic changes in the backscattered energy (CBE) with the increasing of medium temperature. This changes are characteristics of the type of scatterers present in the medium: scattering media composed by scatterers of muscular nature show a decreasing CBE with temperature, unlike scattering media composed by scatterers of lipid nature that show the inverse behavior. This properties where previously studied in order to map medium temperature during ultrasound therapy.

This work aims to the study of a new methodology for non-invasive tissue characterization to potentially provide conventional images with additional information about media. This methodology is based in CBE expressed on intensity variations in conventional ultrasound images when the medium is submitted to a temperature increment. It was possible, using simulated ultrasound signals and images, with Matlab toolbox K-Wave, to develop the new methodology whose results are consistent with theoretical models present in *Straube* and *Arthur* studies, that modulated the expected backscattered energy received by a tissue volume. With data acquired *ex-vivo*, i.e., using samples of porcine muscle and fat, it was possible to obtain distinct CBE signatures for each one of them. These results could be the starting point of a new simple and cheap method for non-invasive tissue classification.

Contents

List of Figures

List of Tables

List of Abbreviations

BE Backscattered Energy

CBE Change in Backscattered Energy

MRI Magnetic Resonance Imaging

CT Computerized Tomography

DXR Digital X-Ray

ROIs Regions of Interest

THI Tissue Harmonic Imaging

SNR Signal to Noise Ration

RF Radio Frequency

FFT Fast Fourier Transform

PML Perfectly Matched Layer

1

Introduction

1.1 Contextualization

Ultrasounds are widely used for medical imaging (Figure 1.1) [13]. This is due to the several advantages over other imaging modalities (e.g., X-ray, computed tomography (CT), magnetic nuclear resonance (MRI), and positron emission tomography) such as [1]:

- Quick and convenient compared to other techniques such as MRI scans, which can take minutes while a ultrasound sweep takes less than a second making it more comfortable to the patient and convenient for real-time study.

- Relatively inexpensive;

- Safety is a major advantage of ultrasound imaging as it does not use ionizative radiation, unlike X-ray or CT scanning, making it very popular for fetal examinations.

- Ultrasound examinations are non-invasive and comfortable to the patient.

However, medical ultrasound images suffer from some problems. One of each is the low contrast resolution since distinct tissues may have similar acoustic impedances as in some soft tissues [12]. In addition, images are usually noisy, specially due to speckle, which lowers image contrast and obscures image details. This makes computer aided diagnosis, such as segmentation or registration, arduous [13]. Penetration depth is also a limitation due to the use of acoustic waves with low energy and also due to the ultrasound attenuation in tissues. To increase examination depth,

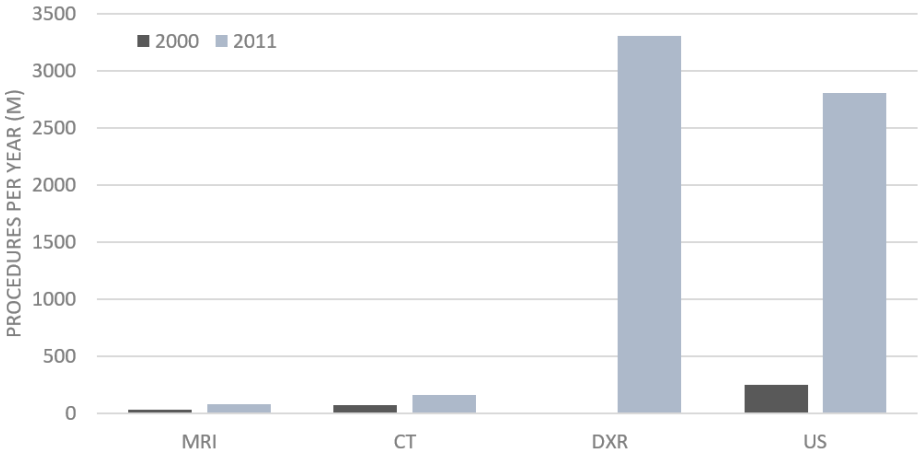

Figure 1.1: *Comparison of estimated number of medical imaging procedures in the world for the years 2000 and 2011 (adapted from [1]).*

a lower frequency must be used causing a loss in axial resolution. High impedance media, such as gas and bones, are also an image artifact origin. In fact for chest examinations radiologists try to position transducer to avoid ribs and lungs. This is why brain scanning with ultrasound is limited and MRI or CT are always preferably chosen. In table 1.1 are listed several characteristics of the main imaging modalities.

Due to these and other ultrasounds imaging problems, in the last years new ultrasound based methodologies have been studied to increase image quality and information provided by ultrasound examinations such as the harmonic imaging, that exploits non-linearities in ultrasound propagation, elastography, that maps tissues stiffness, and Doppler Color Flow Imaging, that assesses blood flow [14][15][16].

Literature also reports studies that have explored multiple acoustic properties with a thermal dependence such as: variations in attenuation, apparent shifting in reflectors localizations (echo-shifting) as well as changes in backscattered energy from sub-wavelength medium inhomogeneities [17]. They conclude that backscattered energy is more robust, easy to quantify and varies monotonously with temperature. In fact, it was reported that media with different scattering content have distinct CBE signatures: media with a lipid scattering content feature a monotonously increasing CBE with temperature, while media with scattering of aqueous nature (as present in muscle tissues) have monotonously decreasing curves [8]. Temperature dependent

Table 1.1: *Characteristics comparison between the most used medical imaging modalities nowadays (adapted from [1]).*

	Ultrasound	**X - ray**	**CT**	**MRI**
What is imaged	Mechanical properties	Mean X-ray tissue absorption	Local tissue X-ray absorption	Biochemistry (T1 and T2)
Acess	Small windows	2 sides needed	Circumferential around body	Circunferential around body
Spatial resolution	Dependent in frequency and depth: 0.2 – 3 mm	~ 1 mm	~ 1 mm	~ 1 mm
Penetration	Dependent in frequency: 3 – 25 cm	Excellent	Excellent	Excellent
Safety	Excellent	Ionizing radiation	Ionizing radiation	Very good
Speed	> 100 frames/sec	Minutes	20 minutes	Typical: 45 minutes; Fastest: 10 frames/sec
Cost	$	$	$$	$$$$
Portability	Excellent	Good	Poor	Poor

changes on backscattered energy were first reported in literature associated with non-invasive temperature estimation for ultrasound therapy purposes, because MRI, a technology used largely nowadays for temperature mapping during ultrasound therapies, lacks portability and safeness.

1.2 Motivation and Objectives

The focus of this thesis is in the physics of a new methodology for non-invasive tissue characterization, to thereby increase the amount and quality of information provided by ultrasounds images. To achieve this, the dependence of changes on backscattered energy (CBE) are explored. The objectives of this thesis are to study the temperature dependence of CBE in both simulated (using k-Wave toolbox) and real data (acquired *ex-vivo*), and therefore verify the possibility of characterize different scattering media and improve conventional ultrasound images. It is intended to compare the results obtained with simulated and real data and evaluate the potential of CBE as a tissue characterization parameter. To the best of our knowledge, temperature dependent features were always viewed as an indicator for temperature

mapping, and never considered for tissue characterization purposes as it is in this thesis. However, results achieved using CBE for temperature mapping are of extremely importance for the achievement of our goal.

1.3 Main Contributions

This thesis reinforces the developments concerning a new technique for tissue characterization using thermo-induced changes on backscattered energy. The two main contributions are:

- Demonstration with data simulated using k-Wave toolbox, that temperature rise induces distinct CBE depending on the medium under analysis;
- Demonstration that it is possible to distinguish different tissue types non-invasively in *ex-vivo* samples.

Part of the work reported on this thesis contributed to the publication of two papers in the proceedings of the 22^{nd} International Congress on Acoustics:

Pedrosa A. , Simões R. J. , Kruger M. A. , Alvarenga A. , Pereira W. C. A. , Teixeira C. A. , On the possiblity of non-invasive tissue assessment using induced changes in backscattered energy: a K-Wave Simulation. Proceedings of the 22^{nd} International Congress on Acoustics, Buenos Aires, Argentina, 5^{th} - 9^{th} September,2016.

Simões R. J. , Pedrosa A. , Pereira W. C. A. , Teixeira C. A. , A complete COMSOL and Matlab finite element medical ultrasound imaging simulation. Proceedings of the 22nd International Congress on Acoustics, Buenos Aires, Argentina, 5^{th} - 9^{th} *September, 2016.*

2

Ultrasounds

Ultrasounds in its standard definition are mechanical waves with a frequency higher than 20 kHz, i.e, out of the human audition range. There are no differences in the physical properties between ultrasounds and audible sounds as they are the same form of energy [18].

2.1 Sound propagation

Sound waves propagate in fluids and solids. Forces acting on the medium molecules cause them to oscillate around their resting positions originating periodic pressure changes in the medium. These perturbations can be transmitted to remote regions from the sound source by interactions between vibrating molecules and their neighbors, i.e., without flow of particles, rather, the effect is transmitted over long distances due to neighbor-to-neighbor interactions. Molecular iterations are indispensable to sound transmission, which explains why sound can not be transmitted through the vacuum [19].

Propagation depends on the intrinsic elastic properties of the medium as well as on its mass density. Both fluids and solids support compression waves, in which the particles oscillate in the direction of wave propagation. This type of elastic waves are called longitudinal waves. However in solids, unlike fluids, the strong binding between particles allows that a shearing strain produced at some point can be transmitted to adjacent layers originating transverse waves. In this type of waves

the particle motion is perpendicular to the direction of propagation [19]. Biological soft tissues are considered viscoelastic solids, where sound propagates essentially due to bulk compression (shear waves are usually neglected because they are highly attenuated for the ultrasonic frequencies usually considered). On other hand, for hard tissues like bone, both compression and shear waves may occur [9][20].

Since a sound wave consists of repeating patterns of high-pressure (compression zones) and low-pressure regions (rarefaction zones) propagating in a medium, it is sometimes referred to as a pressure wave (figure 2.1).

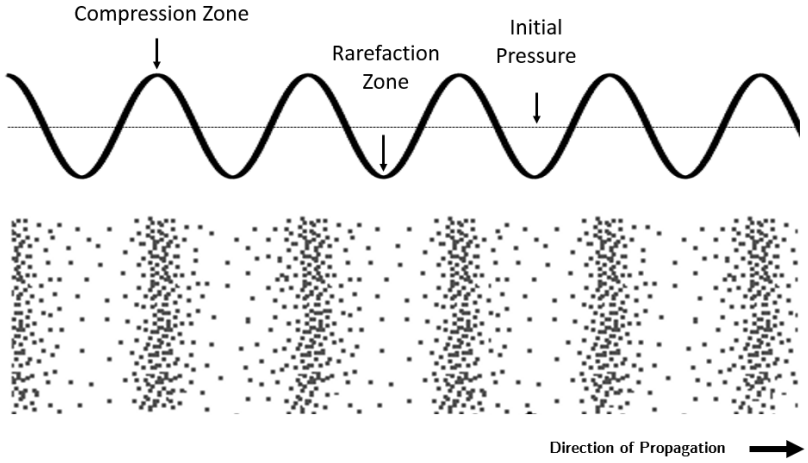

Figure 2.1: *Sinusoidal pressure variation in a fluid at a instant of time. In the next time instant compression and rarefaction zones will shift in the direction of the propagation (adapted from [2]).*

The wave equation for a plane wave propagating can be given by the second-order wave equation, presented in (2.1).

$$\nabla^2 p = \frac{1}{c^2} \frac{\partial^2 p}{\partial t^2} \ , \tag{2.1}$$

where p is the acoustic pressure, c is the sound speed and t the time. Solving this equation for a wave propagating in z direction, we can obtain equation (2.2),

$$p(z,t) = p_0 \ cos(k(z - tc)) \ , \tag{2.2}$$

where k is the wave number and p_0 the normal medium pressure. Wave frequency, f,

is then the number of oscillations per period, given by $f = kc/2\pi$, in Hertz [9]. The speed at which a wave propagates in a medium (c) depends on the medium density, ρ, and compressibility, K. These properties are inversely dependent: a variation in density is usually accompanied by a larger opposite variation in compressibility (2.3), as stated by the following equation,

$$c = \sqrt{\frac{1}{\rho\ K}}\ . \tag{2.3}$$

Because compressibility varies more rapidly, denser materials have usually bigger acoustic velocity [19]. Wavelength (λ) is the distance between two consecutive points in the same vibration state. As velocity is constant for a particular medium, it is a change in the wavelength that follows a eventual frequency shift (2.4):

$$f = \frac{c}{\lambda}\ . \tag{2.4}$$

In table 2.1, the sound speed for multiple materials including biological tissues can be consulted. While in classical mechanics mass and velocity are used to compute the *momentum*, in acoustics mass can be replaced by the material mass per unit volume, i.e, density, and compute the acoustic impedance using the medium sound speed, as stated in equation (2.5) [19]:

$$Z = \rho\ c\ . \tag{2.5}$$

Acoustic impedance is then a physical property of materials. It describes how much resistance an ultrasound beam experiences as it travels in a specific material and is expressed as $kg\cdot s^{-1}\cdot m^{-2}$, a physical unit called $rayl$. In table 2.1 the acoustic impedances of multiple biological tissues can be consulted.

Table 2.1: *Density, ρ, sound speed, c and impedance Z for multiple materials, including biological tissues (adapted from [11] and [12]).*

Material	ρ kg·m^{-3}	c m·s^{-1}	Z kg·m^{-2}·s^{-1} (x10^6)
Air	1.2	330	0.0004
Aluminum	2700	6400	17
Mercury	13600	1450	20
Polyethylene	920	2000	1.8
Water	1000	1480	1.5
Blood	1060	1570	1.62
Bone	1380 - 1810	4080	3.75 - 7.38
Brain	1030	-	1.55 - 1.66
Fat	920	1450	1.35
Kidney	1040	1560	1.62
Liver	1060	1570	1.64 - 1.68
Lung	400		0.26
Muscle	1070	-	1.65 - 1.74
Spleen	1060		1.65 - 1.67

2.2 Interaction with media

Ultrasound waves can interact with media through multiple phenomenons: reflection, refraction, scattering, diffraction, divergence, interference and absorption [19].

Reflection

A difference in acoustic impedances causes some portion of the sound to be reflected at the interface and other to be transmitted to the second medium (figure 2.2.A). The reflection coefficient for beam intensity when traveling from a medium with impedance Z_1 to medium Z_2 is expressed in equation (2.6):

$$\%R = \left(\frac{Z_2 - Z_1}{Z_2 + Z_1}\right)^2 \times 100 \ . \tag{2.6}$$

It can be easily seen that the magnitude of the reflected wave varies directly with the acoustic impedance difference between two media. This allows the detection of media mismatches, which create the major organ outlines seen in diagnostic ultrasound examinations.

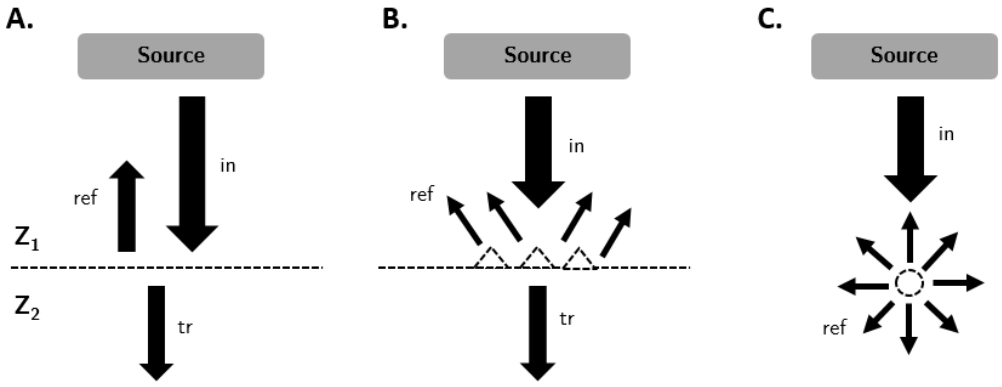

Figure 2.2: *Reflection regimes (in: incident beam; ref: reflected beam; tr: transmitted beam).* ***A)*** *Reflection at a specular interface dividing two different media with impedances Z_1 and Z_2.* ***B)*** *Reflection at a rough surface;* ***C)*** *Scattering of sound by sub-wavelength heterogeneity (adapted from [3]).*

Refraction

In what concerns the transmitted wave, the coefficient is given by equation (2.7). The angle of incidence in the interface is crucial to the direction of transmitted beam. If the sound beam strikes an interface at an angle of 90 degrees (normal incidence), transmitted wave will propagate to the second medium without a change in direction.

$$\%T = \frac{4\ Z_2 Z_1}{(Z_2 + Z_1)^2} \times 100\ . \tag{2.7}$$

However, when the incidence is not normal the transmitted beam will suffer a deflection from the straight-line path. This effect is called refraction and is described by Snell's law, which relates the angle of transmission with the relative velocities of sound in the two media (figure 2.3). If the sound speed is the same for two media, refraction does not occurs, even if the acoustic impedances are different.

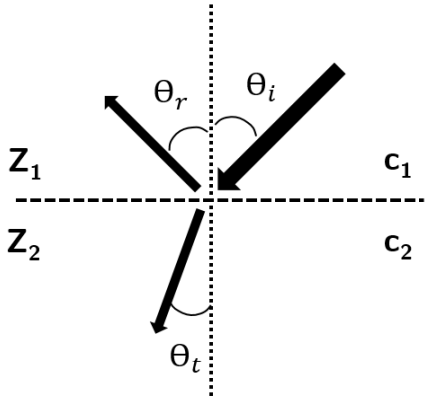

Figure 2.3: *Sound refraction. The reflected beam angle, θ_r, is equal but opposite to that of the incident beam, θ_i. The transmitted beam angle, θ_t, is different from the incident angle and given by Snell Law (2.8). Impedance mismatch, Z_1 and Z_2, defines the beams intensities whereas acoustic speeds, c_1 and c_2, define the angle relation (adapted from [3]).*

$$\frac{sin\ \phi_i}{sin\ \phi_t} = \frac{c_i}{c_t}\ . \tag{2.8}$$

Scattering

Reflection is not always specular as described before. Scattering is a general term that refers to the reflection of sound from not perfectly smooth medium heterogeneities (figure 2.2.B and 2.2.C). It is considered a nonlinear phenomenon because a wave scattered in one scatterer could hit another scatterer and then return to the first one. An important aspect about scattering is that it depends on the ratio between particle dimension, a, and the wavelength, λ, and so different regimes can be considered [20]:

• Specular ($\lambda << a$): if λ is much smaller than the size of the heterogeneity (as happens in large cysts, vessel or organ boundaries), the reflected wave will return to the original without lost of beam phase coherence, in what is called specular reflection (as discussed in Reflection section and illustrated in figure 2.2.A). It does not have a frequency dependence;

• Diffractive ($\lambda \simeq a$): in contrast, a diffracted scattered wave is created if the dimensions of heterogeneities are comparable to the wavelength (small cysts or micro

calcifications);

• Diffusive ($\lambda >> a$) : for scatterers much smaller than the wavelength, which includes for example blood cells, Rayleigh scattering occurs. It depends on the fourth power of frequency and is also proportional to the sixth power of scatterers size. Its coefficient, σ_s, is given by equation (2.9), which applies when wavelength, λ, is larger than $2\pi a$ [8]:

$$\sigma_s = \frac{4\pi k^4 a^6}{9} \left[\left(\frac{K_s - K_m}{K_m} \right)^2 + \frac{1}{3} \left(\frac{3\rho_s + 3\rho_m}{2\rho_s + \rho_m} \right)^2 \right] , \tag{2.9}$$

where k is the wave number, a is the radius of the scatterer, K and ρ are the compressibility and density of the scatterer s and medium m.

Echoes from non-specular reflectors are generally weaker than those returning from specular ones, meaning that scattered signals from soft tissue are considerably smaller than the specularly originated in organ boundaries. However, scattering events can help to access micro-structural properties of the medium such as scatterers size and concentration. In fact, the grainy aspect or echo-structure present in ultrasound images of soft tissues (also denoted as speckle) is highly dependent of scattering events [13][21].

Diffraction

The phenomenon in which ultrasound beam diverges farther from the sound source is called diffraction. The rate of divergence increases as the size (diameter) of the sound source decreases. Diffraction also occurs after the beam with planar sound waves passes through a small aperture (on the order of one wavelength) because wave is blocked everywhere but in the area of the aperture, acting as a small sound source allowing the beam to diverge rapidly [19].

Interference

When multiple sound waves are propagating in the same medium, they interact giving rise to a new wave which is the sum of all individual ones, in a phenomenon named interference. Depending on relative waves phases, constructive or destructive patterns appear. Interference is important in the design of ultrasonic transducers because it affects the uniformity of the beam intensity throughout the ultrasound field. Focusing of the ultrasound beam is also based on the principle of wave interference [19]. Furthermore scattered signals interact constructively and destructively, depending on the their relative phases, originating patterns shown as bright and dark dots in a ultrasound image, a not random noise called speckle.

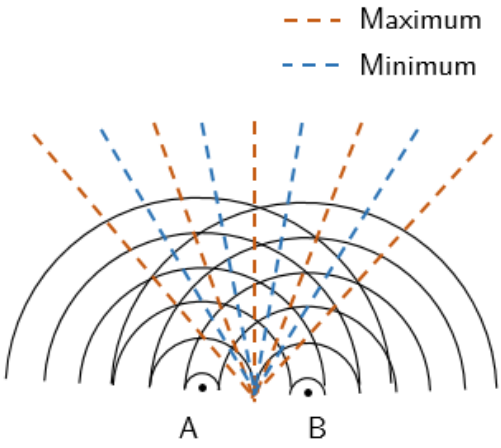

Figure 2.4: *Waves of two sources interact giving raise to regions of maximum intensity, due to constructive interference, and regions of minimum intensity, due to destructive interference (adapted from [4]).*

Attenuation

When propagating through a medium, ultrasound waves loose energy due to scattering and absorption (heat, hysteresis and viscosity) phenomena. This attenuation of the ultrasound beam follows an exponential function (2.10) that includes the effects of both scattering and absorption (figure 2.5):

$$A = A_0 \; exp \; (-\alpha z) \; , \tag{2.10}$$

where A_0 is the initial amplitude of the sound wave, A is the wave amplitude at a distance z from the initial location. The quantity α is the attenuation coefficient of the medium and is given in *nepers per meter* (Np/m) or *decibels per meter* (dB/m). Based on measured data, it appears that the attenuation follows a frequency power law, stated in equation (2.11), where α_1 and y are variables that depend on the predominant scattering regime in the medium (see table 2.2) [22]. The nonlinear parameter, B/A, is related with the waveform distortion when ultrasound beam propagates in a medium [23].

$$\alpha = \alpha_1 f^y \ . \tag{2.11}$$

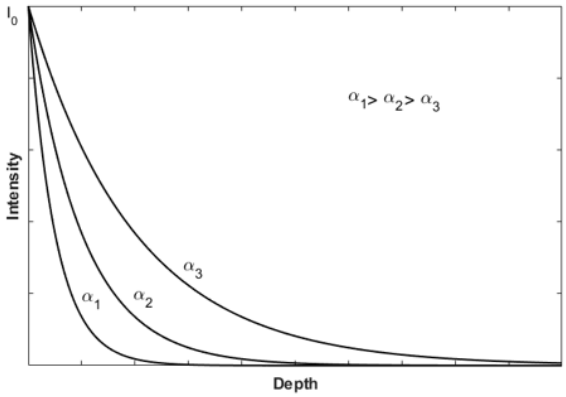

Figure 2.5: *Graphical representation of equation 2.10. Increasing attenuation coefficient, α, intensity damping is faster (adapted from [5]).*

Table 2.2: *Attenuation coefficients α_1 and y and nonlinear parameter B/A of multiple materials (adapted from [12]).*

Material	**α_1 (dB·cm^{-1}·MHz^{-1})**	***y***	***B/A***
Water	0.002	2	5.2
Blood	0.15	1.21	6
Fat	0.6	1	10
Liver	0.9	1.1	1.8
Kidney	1	1	1.5
Brain	0.8	1.35	6.9
Muscle	α = 1.3-3.3 at 1 MHz		7.4

2.3 Medical Ultrasound Imaging

Although industrial applications are common, ultrasounds are mostly known for its use in medicine, mainly for diagnostic imaging. It is used for visualizing structures including tendons, muscles, joints, vessels, internal organs and blood flow studies. Despite the large variety of scanning modes of ultrasonography all share the same basic steps: generation of a beam, reception of the returning echoes and processing of the signal for display. Transducers are crucial instruments as they are responsible for generate and receive the ultrasound beam. Generally, commercial ultrasound imaging devices use frequencies ranging from 1 to 20 MHz (e.g. 3.5 and 7.5 MHz for general abdominal and breast examinations respectively) [5][19].

2.3.1 Ultrasonic Transducers

Transducer refers to a device that converts energy from one form to another. Ultrasonic transducers act both as the source and detector of ultrasound signals, due to a phenomenon called *piezoelectric effect*. This physical phenomenon consists on a change in electric polarization that is produced in certain materials when they are subjected to mechanical stresses. An important feature to note about this phenomenon is that the process is reversible: a deformation of these materials occurs when subjected to an electric field [24]. One important feature related with ultrasonic transducers is resolution.

Resolution

The spatial resolution refers to the minimum distance at which two reflectors (or scatterers) can be and still be identified separately. Essentially it can be divided into:

- Axial resolution (res_{axial})**:** minimum distance that two reflecting targets can stay along the sound beam axis and still be distinguished. This distance is given by equation (2.12). Optimal axial resolution is achieved using short duration acoustic

pulses [25]. Spatial pulse length (SPL) is equals to the wavelength, λ, times the number of cycles used.

$$res_{axial} = SPL/2 \ . \tag{2.12}$$

- Lateral resolution: minimum distance that two reflectors may be along a line perpendicular to the sound beam and yet be seen as separate reflectors. It only depends on the sound beam lateral width. The problem is that the lateral width of a sound beam generated by a transducer (principally by a unfocused one) depend on the axial depth, with two distinct regions usually being defined: a near field (or Fresnel zone), and a far field (or Fraunhoffer zone). The near field gets more uniform and narrow as we approximate to the transition zone. In other hand, beam gradually weakens and diverges in the far field. Beam width varies inversely with frequency [19]. Single-element transducers are focused in order to achieve better lateral resolution. Focusing can be done using a curved piezoelectric element. This means that their focal distance will be set permanently at fabrication. The beam width, W, at focal depth, F, is given by equation (2.13), where a is the transducer aperture and λ the wavelength [19][26],

$$W = \frac{\lambda \ F}{a} \ . \tag{2.13}$$

Transducer arrays

Transducer arrays are used in diagnostic devices rather than single element transducers. An array transducer assembly consists of piezoelectric elements that can be excited individually by sending electrical excitation signals to each one as depicted in figure 2.6 [3]. The emerging beam is the sum of individual beams from each of the elements. The transmitted beam from an array may be focused by introducing time delays at the appropriate sequence to the excitation pulses applied to the elements, something not possible with a single element geometry. This is called beamforming and allows also sending a sound beam in any direction with a static

transducer. The number of elements involved varies with the type of array and the design (linear and annular configurations are the most used). In a linear array the elements are positioned in a straight or curved line. In other hand, in an annular geometry transducer elements are placed concentrically. Although these two designs have different clinical applications, their focusing principles are similar.

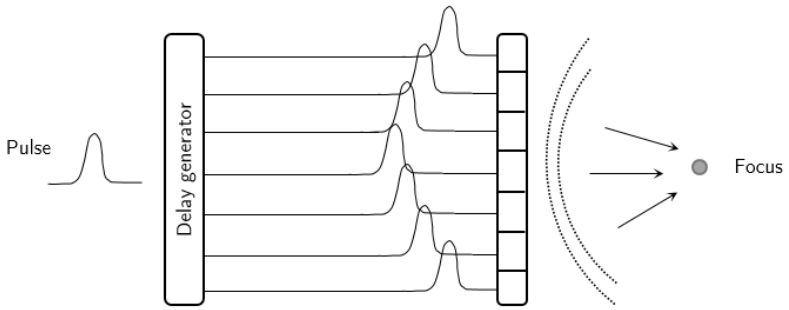

Figure 2.6: *Beamforming of the emitted beam using a system of delays in order to focus emitted beam at a specific depth (adapted from [6]).*

2.3.2 Main ultrasound scanning modes

Nowadays in the medical field, ultrasound inspection is done mainly using a pulse-echo approach: a short duration burst of ultrasonic energy is transmitted into the medium and echoes from scatterers and interfaces are detected and displayed. The distance, d, from the transducer to a reflector can be determined from the time travel, t, between the pulse emission and the echo signal reception, stated in equation (2.14), knowing the medium sound speed c. This equation is sometimes referred as the echo range equation:

$$d = 1/2 \; c \; t \; . \tag{2.14}$$

One problem that must be considered is the attenuation of an ultrasound beam with depth. Equally reflective interfaces produce different signals levels, depending on their relative distances from the transducer. It is often advantageous to display reflectors of similar size, shape, and reflection coefficients with equal signal strengths or brightness levels. Exponential amplification, or time gain compensation (TGC),

are used to correct the signals for attenuation [3]. This is done increasing signal amplification exponentially with depth.

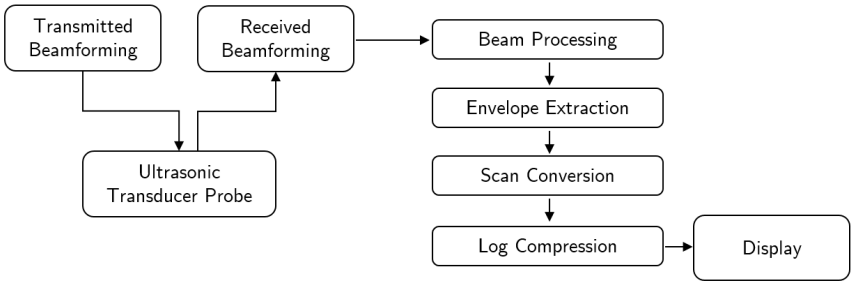

Figure 2.7: *Principal functional components of an ultrasound imaging system (adapted from [5]).*

Other processing steps include the beamforming of the received echoes and the extraction of signals envelope. Finally, signals are logarithmically compressed, which refers to the reduction of the amplitude range of echo signals to a given range of echo amplitudes. To the range of signals amplitude that an instrument is capable of handling is called the dynamic range. A block diagram showing the basic functional components of an ultrasound imaging system is presented in schema of figure 2.7.

A-mode

A-mode scanning, which stands for amplitude mode, is an one-dimensional representation of the signal amplitude versus depth [3]. Ultrasound beam is directed along a single path and knowing material sound speed or making approximations it is possible to know their respective depth using the echo ranging equation 2.14. Thus amplitude of A-scan signals convey the strength of detected echoes generated at interfaces that lie along the line of sight (or scan line) and their arrival time. In clinical environment, A-Mode is used for detection of mid-line shift, and for localization of extraneous bodies in the eye. Out of medical applications its widely used in industry for non-destructive testing of materials [19].

B-mode

A B-mode, or brightness mode display, is a 2D image, capable of representing tissues and organ boundaries within the body [27]. It is formed from a large number of A-mode lines. This means that each line in the image is produced by a pulse–echo sequence. The image brightness at each point is related to the strength and depth of the echo. B-Mode image is done sweeping the window of activated elements in the transducer [3]. One complete sweep may take $1/30^{th}$ of a second, meaning that a considerable amount of images can be formed in less that a second. Therefore, B-mode allows real-time imaging, i.e, with a negligible delay, unlike other imaging techniques such as CT scan or MRI.

M-mode

A motion-mode image, or M-mode, is a ultrasonographic imaging modality that allows the tracking of interface movement. The transducer is placed in a static position and a single line is visualized. Converting this line of sight into brightness dots, and adding a time dimension, it is possible to create a 2D image that represents the interfaces movements through time. Stationary reflectors trace out a straight line on such a display, whereas moving reflectors trace out oscillatory lines. Due to the good temporal resolution it is appropriate to detect and record rapid movements. M-mode is frequently used in echocardiagraphy to evaluate the movement of heart walls and valves and also to measure chamber dimensions and heart debits. A correlation with other physiologic signals such as ECG and respiratory signals can also be made [19].

2.3.3 Other medical ultrasound methodologies

Doppler

Doppler ultrasound equipment is useful for detecting and characterizing reflectors or scatterers motion [3]. Doppler effect refers to a change in the frequency of sound

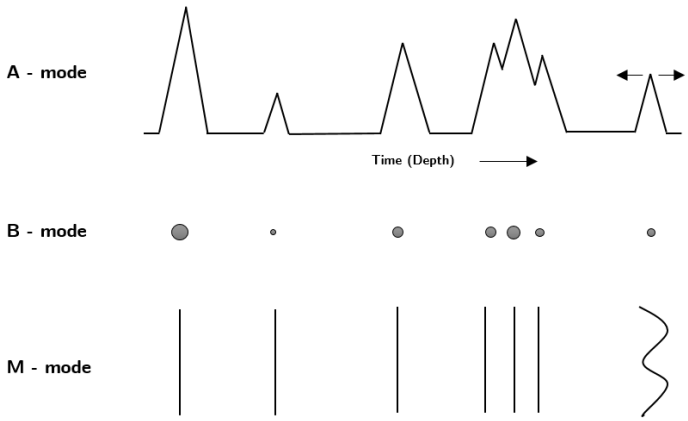

Figure 2.8: *Different display modes of ultrasound (adapted from [3]).*

signals when there is a relative motion between the source and receptor of the waves. The difference between the received and the emitted frequency, f and f_d respectively, is called Doppler frequency, f_d. It is related to a object velocity, v_b, by equation (2.15) [5]. Therefore, if the object is moving toward our away the source the received frequency will be greater or smaller than f_s, respectively. Thus, ultrasonic Doppler is used to detect motion of body structures such as heart valves and fetal heart walls but also to assess blood flow in arteries and veins [3].

$$f_d = \frac{2\ v_b\ cos(\theta)}{c}\ f_s\ , \tag{2.15}$$

where f_s is the source frequency, f_d is the Doppler frequency ($f_d = f - f_s$), v_b the object velocity and $cos(\theta)$ the relative angle between sound beam and object movement.

Elastography

Elastography is a state of the art ultrasound technique that highlights tissue stiffness, just like the traditional palpation method, in order to distinguish the soft and hard sites of a medium [15]. Palpation is a subjective approach that requires a direct contact and can only be applied to superficial organs. Elastography consists on the tissue movements evaluation when an external force is applied. These dis-

placements can be compared with the original tissue length supplied by the B-mode images. An estimative of the *Young* modulus, E, the physical parameter corresponding to the stiffness, can be made due to relation between stiffness and strain: $E = stress/strain$ [2]. The *Young* modulus exhibits variations between different biological tissues, which makes it ideal for the characterization of different tissues with a good contrast. This technique is a good tool to characterize breast tumors and also for diagnosing liver fibrosis.

Tissue Harmonic Imaging

Harmonic imaging (THI) is a technique that provides images with better quality, than the conventional ultrasound, by exploring the non-linear propagation of ultrasound in the body tissues [14]. Harmonics are generated while the pulse propagates through tissue because the high pressure portion of the wave travels faster than low pressure, resulting in wave shape distortion. This change in waveform leads to generation of harmonics. Higher harmonics suffer more attenuation, and so harmonic imaging uses the second harmonic [5]. THI shows a decreased reverberation and side lobe artifacts, increased axial and lateral resolution, increased SNR and improved resolution in obese patients [28].

2.4 Therapeutic Ultrasound

Due to its capability to induce biological effects by depositing energy in tissue, ultrasound has been studied and used as a therapeutic solution as well. In diagnostic ultrasound safety is a major feature, thus the likelihood of bioeffects are kept relatively low (or negligible) due to the use of pulses with limited intensities and short exposure durations. But increasing power or intensity of ultrasound beams, the probability of inducing biological effects increase as well [29]. Effects are essentially of thermal nature but non-thermal effects are reported as well, e.g. ultrasonic cavitation, mechanical stress, etc. [30].

2.4.1 Thermal Mechanisms

Heating is one of the results of the absorption of ultrasound energy in biological tissue. Therapeutic applications of ultrasound heating utilize longer durations of excitation with unfocused beams, or use higher intensity focused ultrasound in shorter periods of time [29].

Physiotherapy

Using unfocused beams, highly absorbing tissues as tendons, can be heated to enhance injuries healing and improving blood flow. It is used for conditions such as bursitis of the shoulder or tendinitis. The ultrasound coupling gel can also include various compounds for enhancing the treatment. Ultrasound pulses help the dermal absorption of the compound (phonophoresis) [29].

Hyperthermia

Ultrasounds can lead to irreversible tissue changes due to heating. This principle is explored by hyperthermia, a treatment for cancer and lesions in which tissues are subjected to cytotoxic temperatures (about 42 °C or more) for periods of approximately 1 hour. Apparent tumor growth reduction is related to this technique. Normally pulse frequencies ranging from 1 to 4 MHz are used [29][31].

High Intensity Focused Ultrasound

High intensity focused ultrasound (HIFU) is a therapeutic technique that takes advantage of the capability to focus energy centimeters away from the transducer. Ultrasound frequencies used ranged from 0.5 to 7 MHz. Uterine fibroids, cardiac and visceral soft tissue ablation, eyebrow lifting are among the potential applications [29][7]. As HIFU applications involve delivery of substantial ultrasonic energy to localized areas, undesired tissue injury is always a possibility. In fact, contemporary ultrasound equipment has the theoretic capability to cause a tissue temperature

increase greater than 4°C at the focal point [32]. It is therefore, very important to accurately determine the location of treatment area. Two technologies were considered for image guidance and monitoring during treatment: magnetic resonance imaging (MRI) and ultrasound [29].

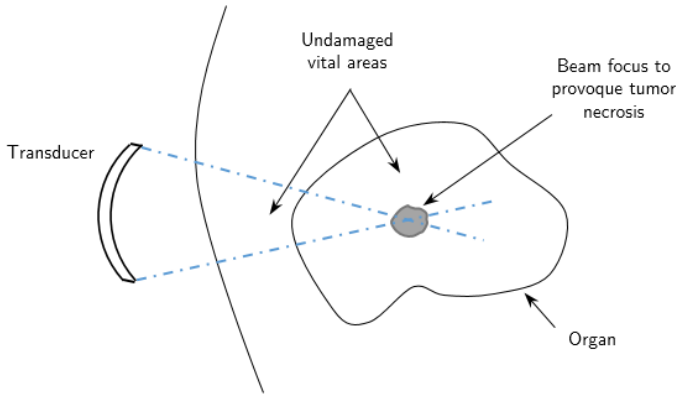

Figure 2.9: *Schema representing fundamentals of HIFU (adapted from [7]).*

2.4.2 Non-Thermal Mechanisms

Ultrasound energy creates also mechanical forces independent of thermal effects. Lithotripsy, cavitation and kilohertz-frequency ultrasound devices are among some non thermal techniques used. Cavitation for example results of the interaction of ultrasound with gas bubbles causing a potentially rapid increase in their number and size. This could lead to mechanical stress on tissues and thereby could cause fluid precipitation and generation of free radicals [33].

2.5 Change in Backscattering Energy

Therapeutic ultrasound approaches, such as hyperthermia and HIFU, highlighted the limitation on methods for measuring temperature with reasonable resolution. This led to a growing number of studies whose objective was the temperature mapping using ultrasound. To achieve this goal some characteristics of the received

signal must have a temperature dependence. The first proposals have attempted to obtain a velocity map of the medium, to enable the calculation of the temperature distribution [34]. From the starting line faced the problem of having to measure both the distance and time or use two transducers positioned in different locations [8]. Current methods lays essentially in three major groups [17]:

a) Methods based on the measurement of acoustic attenuation coefficient. This methodology faced the problem of very small attenuation variation for temperatures up to 50°C, clearly out of the suitable range for human physiology;

b) Methods based on echo shifts, due to thermal expansion and changes in sound speed: although this technique showed to be a promising way of temperature estimation, it proved to be a hard task because prior knowledge of sound speed and expansion coefficients are required. Furthermore the high sensibility to undesired movements is difficult to eliminate.

c) Methods that exploit changes in backscattered signals from a volume of scatterers. *Straube et al.* in [8] start to study the CBE in tissue regions with inhomogeneities (scatterers) for temperature mapping because no prior knowledge of temperature dependent sound speed is needed. Although scanners provide a visual representation or texture of the tissues, usually no quantitative criteria are derived from backscattered echoes and so potentially useful information is discarded.

2.5.1 CBE - Theoretical model

Sigelmann and Reid developed a theoretical model (2.16) to compute the average backscattered power received from a small random scattering volume, in response to a sinusoidal burst [8][35]:

$$P_r(T) = \frac{2H^2\delta}{8R^4\alpha(T)}\ \eta(T)\ S(1 - e^{-2\alpha(T)c(T)\tau})\ \left[\frac{e^{\alpha(T)c(T)\delta} - e^{-\alpha(T)c(T)\delta}}{2\alpha(T)c(T)\delta}\right] . \qquad (2.16)$$

where H and δ are the amplitude and duration of the ultrasound pulse respectively, S and τ the cross section and thickness of the scattering volume respectively, R

the distance between the transducer and the scattering volume, and $\alpha(T)$, $c(T)$ and $\eta(T)$ are the attenuation, sound speed and backscattering coefficient temperature dependence functions within the volume, respectively. The term in square brackets is nearly unitary and varies less than 5%, for a change of $\alpha(T)$, $c(T)$ or δ by a factor 10 [8]. It was proposed the normalization of this model to the power received at a baseline temperature (T_R), for example human body temperature (i.e, 37°C), eliminating non thermal-dependent parameters and highlighting the change on backscattered power received [8]:

$$CBE(T) = \frac{\alpha(T_R)}{\alpha(T)} \frac{\eta(T)}{\eta(T_R)} \frac{[1 - e^{-2\alpha(T)x}]}{[1 - e^{-2\alpha(T_R)x}]} \ , \tag{2.17}$$

where x is the medium thickness. It is possible to observe in equation (2.17) that CBE depends on the temperature dependence of attenuation, $\alpha(T)$, and backscattering coefficient, $\eta(T)$. Expression (2.17) can be simplified assuming that for the temperature range 37 to 50 °C [8]:

- The wave number, $k = 2\pi f/c(T)$, varies less than $< 1.5\%$ [17];

- Change of only 0.27 dB on the normalized backscattered power (at $50°C$) due to attenuation (graphic 2.10) [8];

- Density is independent of temperature because is expected to have a small variation and no data is available in literature [8];

- Backscattering coefficient for a distribution of scatterers, η, is proportional to the scattering coefficient of a single one, σ_s, given by equation 2.9.

Thus, *Straube et al.* were able to obtain equation (2.18), where ρ and c are the density and sound speed of the scatterer. Indexes s and m denote scatterer and medium properties, respectively. This equation states the major dependency of the changes in backscattering energy with the sound speed temperature dependence (in

the temperature range defined):

$$CBE = \frac{\eta(T)}{\eta(T_R)} = \frac{\left(\frac{\rho_m c_m(T)^2 - \rho_s c_s(T)^2}{\rho_s c_s(T)^2}\right)^2 + \frac{1}{3}\left(\frac{3\rho_s - 3\rho_m}{2\rho_s + \rho_m}\right)^2}{\left(\frac{\rho_m c_m(T_R)^2 - \rho_s c_s(T_R)^2}{\rho_s c_s(T_R)^2}\right)^2 + \frac{1}{3}\left(\frac{3\rho_s - 3\rho_m}{2\rho_s + \rho_m}\right)^2} . \tag{2.18}$$

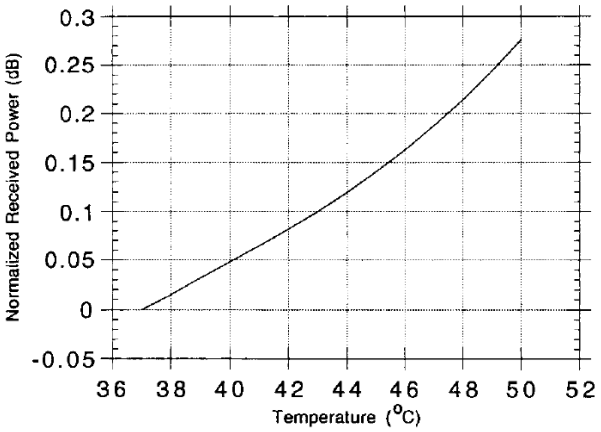

Figure 2.10: *Change in backscattering energy due to attenuation dependency with temperature. Only a 0.27 dB variation is observed at 50 °C (extracted from [8]).*

2.5.2 Temperature-dependent sound speed

Previous studies have empirically characterized the dependency of sound speed with the temperature in multiple biological media. In *Straube et al.* work it is possible to find the characterization of two media that have distinct scattering content: muscle tissue (medium constituted predominately by aqueous scatterers), and fat (medium predominately composed by lipid scatterers). In the expressions below the polynomial coefficients obtained in their experiments are presented [8]. The sound speed in high water content tissues decreases with temperature (2.21), on the other hand, the sound speed in high lipid-content tissues increases with increasing temperature (2.20). In expression (2.19) is the temperature dependency of sound speed for a water medium [36].

$$c_{water}(T) = 1471.4 + 3.9979T - 0.03513T^2 \tag{2.19}$$

$$c_{lip}(T) = 1471.4 + 3.9979T - 0.03513T^2 \tag{2.20}$$

$$c_{aq}(T) = 1810.7 - 13.892T + 0.10160T^2 \tag{2.21}$$

Concluding, CBE depends mainly on the changes in sound speed. It is then possible to use the presented polynomials and compute the expected changes in backscattered energy. Graphic of figure 2.11 shows the theoretical CBE for lipid (ρ = 960 kg/m^3) and aqueous (ρ = 1060 kg/m^3) scatterers in a water medium background. CBE is monotonously positive for lipid scatterers and negative for aqueous ones. Theoretically it is then expected that CBE varies monotonically with temperature and assume different behavior, depending on the scatterers type and background medium.

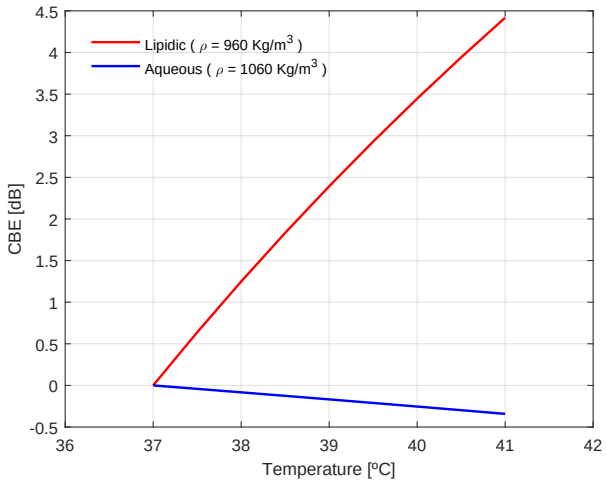

Figure 2.11: *Theoretical CBE curves (see equation 2.18) for a water medium containing: lipid scatterers with a density of 960 kg/m^3 (red line) and aqueous scatterers with a density of 1060 kg/m^3. It is expected a change of 4.5 dB and -0.4 dB in backscattered energy, respectively for lipid and aqueous scattering media, when the temperature increases from 37° to 41°C.*

Another important aspect is that the dispersion of the velocity is the only frequency dependent factor of the normalized backscattered coefficient. However the change in sound speed over the frequency range from 1 to 10 MHz is less than 1% for tissues which means that CBE is expected to be relatively independent of frequency [8].

3

Methods

This work was based on two main approaches. First a set of simulations were conducted to simulate changes in backscattered energy with temperature, in A-scan signals as well as in B-Mode images. It is expected to understand the fundamental principles and physics behind the proposed technique. Secondly, real data acquisition and analysis were accomplished in *ex-vivo* tissues samples.

3.1 Simulation Setup

In the last century progresses in computational power have lead to the possibility of modeling and simulate scientific problems in a realistic way. This has offered the chance of getting an insight to real scientific problem solutions that otherwise were insoluble by traditional means or difficult to study in a laboratory.

3.1.1 k-Wave: an open source Matlab toolbox

Concerning acoustic, multiple simulation softwares have become popular such as *FieldII*, *Focus* and *Comsol* [37][38]. Actually *FieldII* seems to be popular among literature in what is related to CBE studies [39][40]. In this work, and after a brief benchmark between these softwares, a MATLAB open source toolbox for time-domain simulation, *K-Wave*, was chosen [36]. Using a MATLAB script, the toolbox functions can be called to design the wanted simulation in a flexible and user friendly environment. The main functions in the toolbox (kspaceFirstOrder1D,

kspaceFirstOrder2D, kspaceFirstOrder3D) solve the coupled first-order system of equations, presented below, rather than the equivalent second-order equation presented in (2.1):

$$\frac{\partial u}{\partial t} = -\frac{1}{\rho_0}\nabla p \ , \tag{3.1}$$

$$\frac{\partial \rho}{\partial t} = -\rho_0 \nabla \cdot u \ , \tag{3.2}$$

$$p = c_0^2 \rho \ , \tag{3.3}$$

where u is the particle velocity, p the acoustic pressure, ρ is the acoustic density, ρ_0 the density at equilibrium and c_0 the sound speed at equilibrium.

Solving Method: K-space method

In a traditional approach, using a finite difference solver, spatial gradients are computed locally based on the function values at neighboring grid points (figure 3.1.A). The more points used, the higher the degree of polynomial required, and the more accurate the estimate of the derivative (Figure 3.1.B). However the size and complexity of the computational grids required increase as well. k-Wave solves the equation system, presented above, using a k-space method (Figure 3.1.C). This combines the spectral calculation of spatial derivatives, using the Fourier allocation method, with a temporal propagator expressed in the spatial frequency domain or k-space. Thus, as uses all data in the fitting, this method is considered global, rather than local (figure 3.1.C). There are two significant advantages in using *Fourier* series: 1) the amplitudes of the *Fourier* components can be computed efficiently using the fast *Fourier* transform (FFT): 2) the basis functions are sinusoidal, so only two grid points per wavelength are theoretically required, rather than the six to ten needed in other methods [9].

To reduce computational time and memory it was taken the option of designing 2D simulations instead of 3D. kspaceFirstOrder2D, the toolbox function that allows to simulate the time-domain propagation of compressional waves through a two-dimensional acoustic medium, receives four input structures: grid, medium, source, and sensor that are more detailed explained in the sections that follow [9]. The definition of this four variables allowed the design of the desirable acoustic simulation.

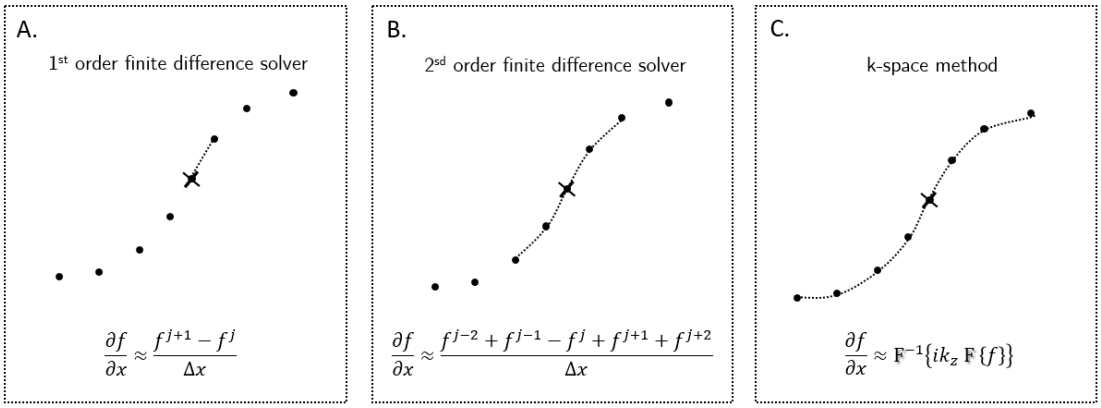

Figure 3.1: *Calculation of spatial gradients using local and global methods.* **(A)** *First-order accurate foward difference.* **(B)** *Fourth-order accurate central difference.* **(C)** *Fourier allocation spectral method (adapted from [9]).*

3.1.2 Grid properties

The computational grids used in the simulations have to be defined both in space and time domain. Grid properties were maintained constant through out all the simulations.

Spatial Grid

Spatially the grid consisted of a 25 by 25 mm square with a mesh grid of 1024 by 1024 points as presented in figure 3.2. To prevent waves to be reflected at simulation boundaries a perfectly matched layer (PML) is added to work as an absorbing boundary layer: a PML of 80 grid points was usually added in all boundaries.

Temporal Vector

Temporal features are also crucial properties of the simulation. Total simulation time was chosen to be approximately 3.6 ms, allowing the detection of an obstacle placed at 27.5 mm from the transducer (considering a sound speed of of 1531 m/s). This means that in our simulations all echoes should be detected as the total depth of the piece is 25 mm. Although k-wave allows time step to be selected by the user it was chosen to be automatically calculated, and a value of 5.67 ns was attained.

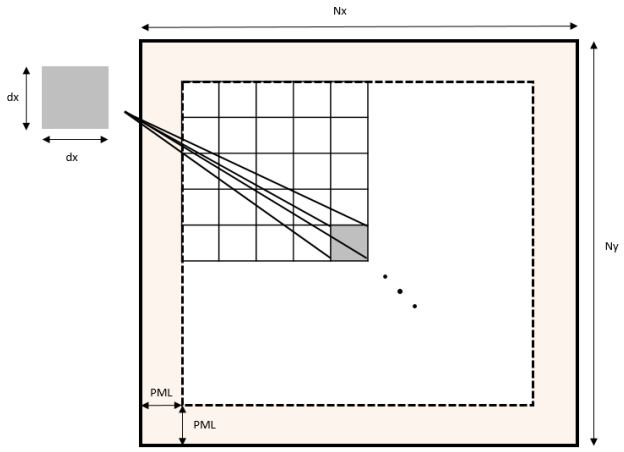

Figure 3.2: *Computational spatially grid used in simulations. Nx and Ny are equal to 1024 points, and PML is equal to 80 grid points in every boundary. Element length is then* $dx = 28.9\ \mu m$.

3.1.3 Medium

The medium definition consisted in a set of matrices with the same size of the grid, defining the acoustic properties at each point of the grid (such as sound speed, density and attenuation). This is a major advantage of k-wave because allow a big flexibility in the design of the simulations.

Background

Water was chosen to be the background material because its acoustic properties are similar with soft tissue. As a fluid, absorption follows a frequency power law. Table

3.1 contains its properties [12]. Attenuation was considered to be the same in all medium.

Table 3.1: *Properties of the background medium, i.e, water (adapted from [12]).*

Material	Value
SOS (c)	$c_{water}(T)\ m/s$
Density (ρ)	1000 kg/m^3
Power law prefactor (α_0)	0.0002 dB·cm^{-1}·MHz^{-1}
Power law exponente (b)	2
Nonlinear parameter (B/A)	5.2

Scattering Content

Since the goal of these simulations is to visualize variations on the backscattered energy, described by equation (2.18), a circular shaped region with a random distribution of scatterers is included. Scatterers are punctual grid points with a cross section, a, equal to 28.94 μm in order to ensure that the statement $\lambda > 2\pi a$, which is a necessary condition imposed by equation (2.9), is followed (for frequencies inferior to 8.5 MHz). Scatterers were spread randomly in accordance with an uniform discrete distribution.

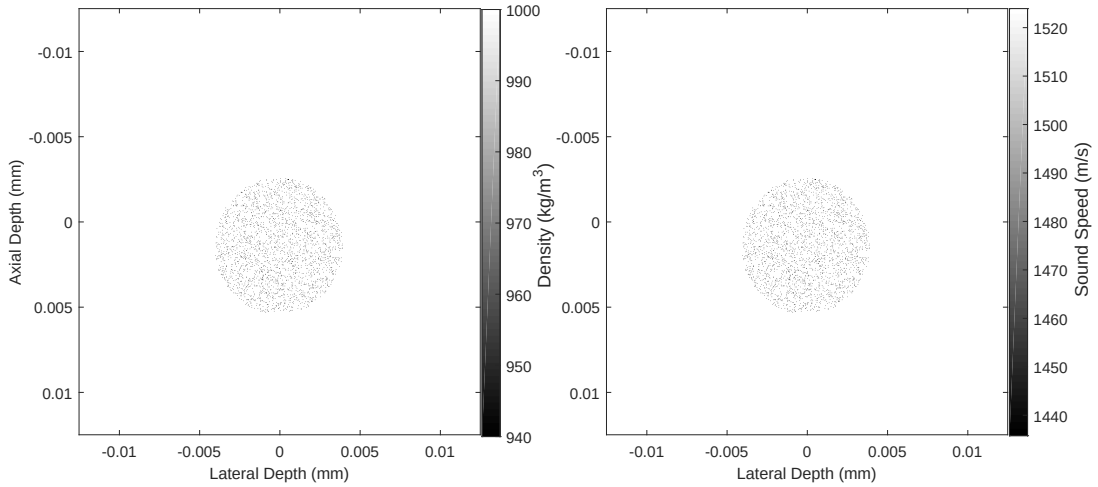

Figure 3.3: *Maps of density (at the left) and sound speed (at the righ) of a designed phantom. Scatterers are placed randomly within a circular region with a radius, in this case, equals to 4 mm.*

These punctual grid point scatterers are basically locals with different density and sound speed (figure 3.3). In this work two scatterer types are used: aqueous (typical of muscle) and lipidic typical of (fat tissues). This choice was made based on the data available in the literature. Their acoustic properties are resumed in table 3.2 and were taken from literature.

Table 3.2: *Properties of the scatterers. Density was changed between simulations depending on simulation goal.*

Scatter type	ρ **kg/m^3**	$c(T)$ **m/s**
Aqueous scatter (muscle)	1020 - 1080	$c_{aq}(T)$
Lipid scatter (fat)	920 - 980	$c_{lip}(T)$

3.1.4 Source and sensor

Source and sensor define the points used to send the excitation pulse and record the acoustic field at each time step during the simulation, respectively. Sensor and source elements were located in the same grid points, just as a real ultrasonic transducer. The acoustic field values are returned as a time series vector for each sensor point. The simulated transducer consisted of an array with 128 elements, each element being a grid point (it was positioned at the top of the grid). Focusing was achieved using toolbox function focus, that returns the appropriate time delays required to focus the signals at a desired position. Focal depth was set to 12.5 mm, the phantom center (where scattering regions are positioned). No apodization is used to form the emitted beamforming. Concerning the beamforming at the reception, the recorded data in a single scan line (RF line) is formed by summing signals from each sensor element (3.4.b) with a *Hanning* apodization, as ilustrated in figure 3.4.A. In figure 3.5 is presented the acoustic field of the transducer when a 4 cycle burst, with a frequency of 7.5 MHz is used. These burst features were the most used through out the simulations just as frequently viewed in literature. As can be see, the maximum intensity of the acoustic field is located at the center of the phantom.

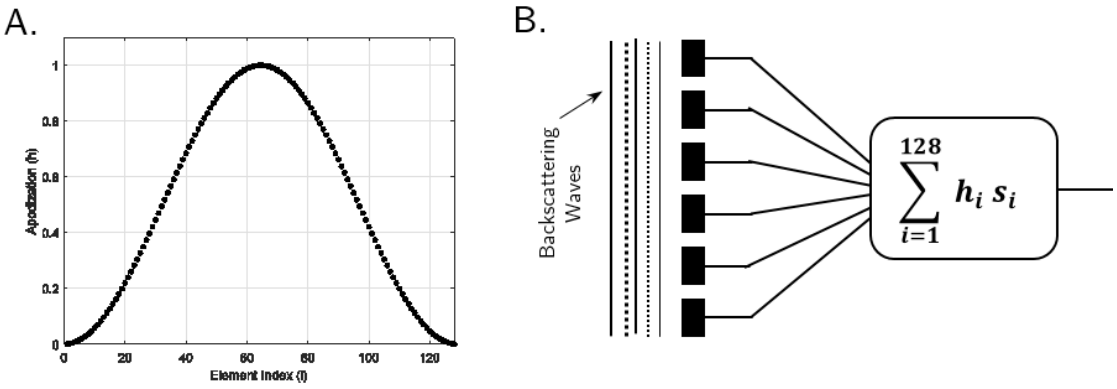

Figure 3.4: A) *Apodization: a Hanning window is used to compute sum gains of each transducer element.* **B)** *Beamforming in the reception.*

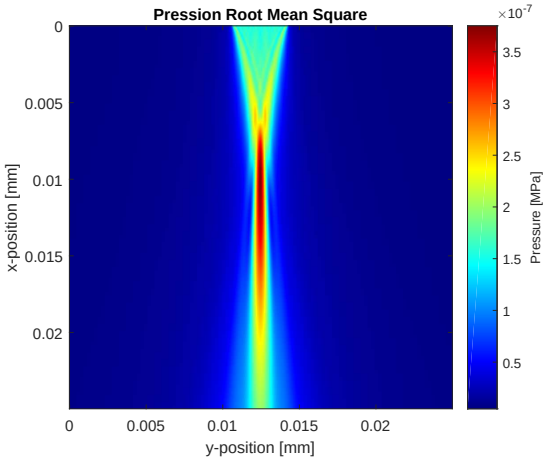

Figure 3.5: *Acoustic field for a 7.5 MHz source. Field is stronger in the focus zone, set to the phantom center, i.e, focal depth equals to approximately 12.5 mm*

3.1.5 Signals Post-Processing

Regarding the RF signals post-processing, it was followed a traditional approach as lightly presented in the scheme of figure 2.7. First as the source and sensor are defined in the same points and as the pressure recording began at the same time as emission is necessary to remove the excitations pulses. Secondly due to attenuation, a time gain compensation (TGC) is also applied. A fourth order *Butterworth* filter is applied with the same center frequency as the excitation burst frequency. Hilbert transform is applied to extract signal envelope. Finally to reduce the dynamic range

of the signals logarithmic compression is applied.

3.1.6 Temperature Variation

A key element in our simulations was the temperature induced changes on backscattered energy. So, in order to simulate the temperature variation, acoustic properties like sound speed, density, and attenuation have to be update along the temperature increasing. However, as described on previous chapter, in a temperature range of 37°C to 41°C changes in density and attenuation due to temperature are small and thus can be negligible in our simulations. Thereby only sound speed was updated, using the polynomial functions (2.19), (2.20) and (2.21). Their graphical representation are presented in figure 3.6. In this phase, to decrease simulation times, and as appropriate results have been observed using a narrower range, temperature was varied between 37° and 41°C in 0.5°C steps.

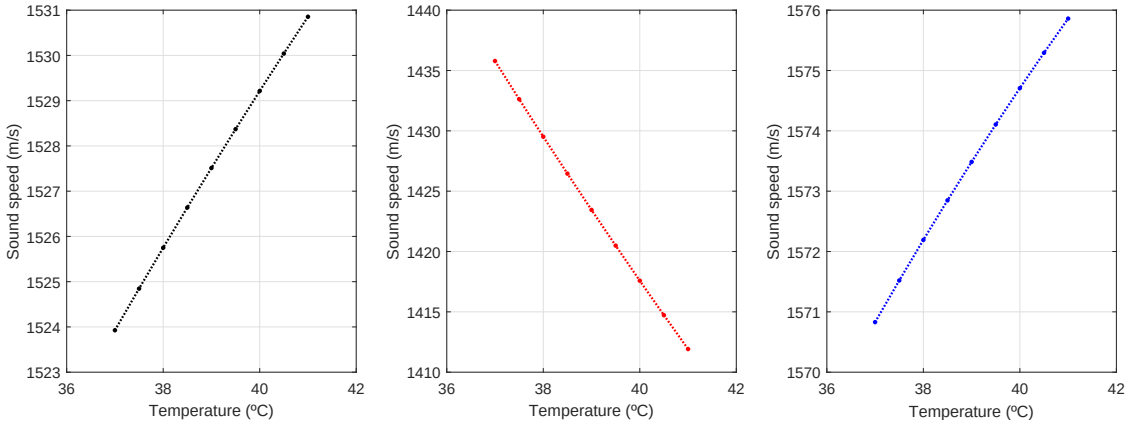

Figure 3.6: *Sound speed variation for a water medium (left), and for lipid (middle) and aqueous (right) scatterers. Calculate using 2.19, 2.20 and 2.21 respectively from left to right.*

3.1.7 A-scan signals simulation

Tracking backscattering energy along a temperature variation was first done in A-scan signals. Two different media were considered: one with lipid scattering content and other with aqueous scatterers. A RF signal is then registered in a line sigh

passing through the scattering region, for each of scattering media (figure 3.7). Temperature is varied and CBE for each medium is computed. This methodology was followed to assess the CBE dependence with variables such as pulse frequency, scatterers concentration (number of scatterers per mm^2) and the density, ρ, of the scatterers.

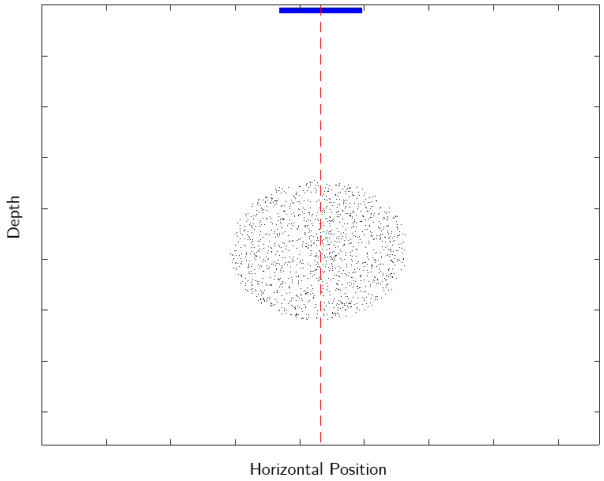

Figure 3.7: *Density map of a phantom containing a lipid scattering region. Blue line at the top is the transducer and the dashed red line represents the line of sight of A-scanning.*

An important aspect of using CBE is that the required signals can easily be measured with a single transducer [8]: calculus of backscattered energy (BE) requires only signals envelope to be squared and summed (3.4). This is done for each temperature, and backscattered energy received at a temperature T can be logarithmically normalized in relation to the backscattered energy received at a reference temperature T_R as stated by equation (3.5) where x is the signal envelope, n signal length, and i a signal sample:

$$BE = \sum_{i=1}^{n} |x(i)|^2 \ , \tag{3.4}$$

$$CBE = 20 \ log_{10} \ BE(T)/BE(T_R) \ . \tag{3.5}$$

Therefore these results for CBE calculated using simulated data can be compared with the theoretical results given by (2.18).

3.1.8 B - mode simulations

B-mode simulations were slightly different from the previously presented. In order to understand if it is possible to detect distinct CBE signatures in a typical B-Mode image, different scattering content were placed in the same medium defined in well detached regions (figures 3.8 and 3.9). Small fluctuation in the background acoustic properties was added to provide the simulated image with the noise typical of a real B-mode image. This was done by picking random grid points and increase their density and sound speed by 10 units, i.e., ρ =1010 kg/m^3 and $c = c_{water} + 10$.

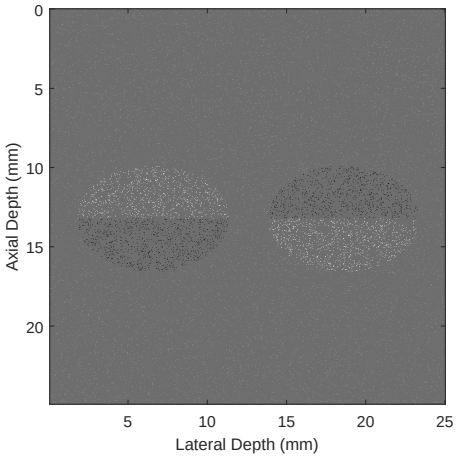

Figure 3.8: *Phantom for simulation of B-mode images. Two disks are placed at a central depth, each one being separated in different scattering content halves. Small variances in properties of background medium were added to give the noise aspect of real images.*

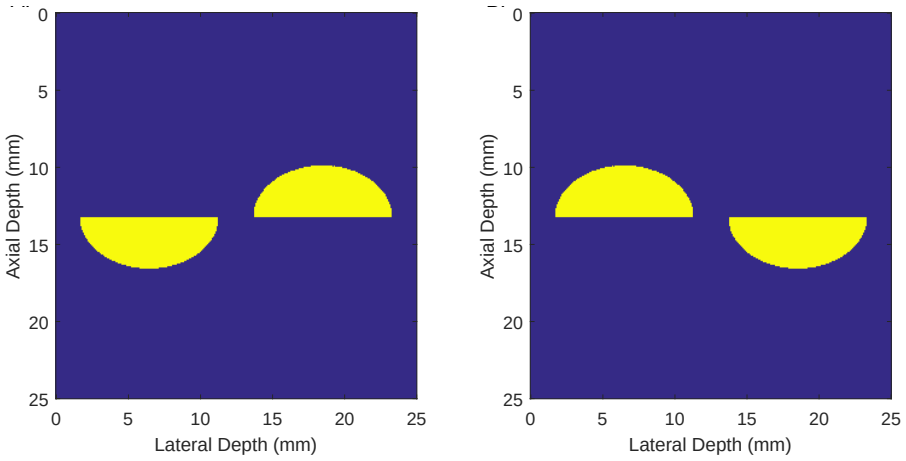

Figure 3.9: *Different scattering media present in simulation.* **A)** *Regions of lipid scattering medium (scatterers density equal ρ = 950 kg/m^3);* **B**) *Regions of aqueous scattering medium (scatterers density equal to ρ = 1065 kg/m^3)*

B-mode image construction is done by sweeping transducer along 600 scanning lines. This number seems bigger than the accomplished in real instrumentation (around 200) but it was necessary in order to guarantee the visualization of both disk regions in the final B-mode image. A burst with frequency of 7.5 MHz was used. An image is generated for each temperature from 37° C to 40° C in 0.5°C steps, forming a volume of 7 images. CBE analysis is done by following gray-level changes on B-mode images. Furthermore new parametric mapping can be formed taking the coefficients of a linear fit applied to the pixel intensity change, as accomplished in previous studies and shown in figure 3.10 [10].

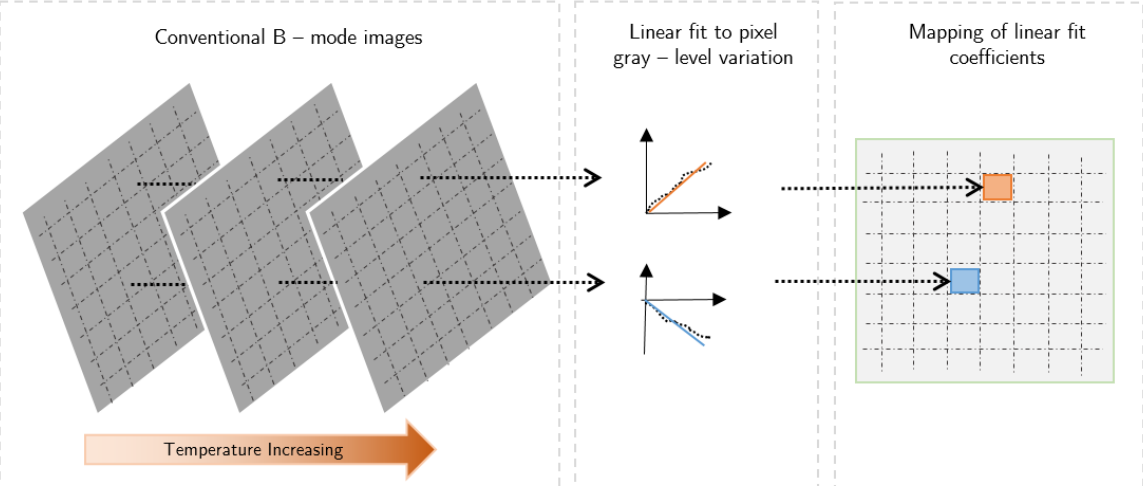

Figure 3.10: *Thermo responsive image construction. A polynomial fit is applied to the pixels intensities (adapted from [10]).*

Slightly differences on media sound speed between images acquired at different temperatures cause distinct speckle patterns. Thus, we considered an algorithm to reduce speckle noise in ultrasound images before analyzing the CBE. The algorithm, developed by *Preetha et all* [41] consists of 5 essentials steps:

i) Image smoothing with a median filter: a circular window was used rather than a square one to avoid blocking artifacts. Window radius was set to 15 pixels as suggested by authors.

ii) Destructive interference smoothing: for each pixel, the maximum value between the median filtered image and the speckled image is selected, to suppress gray values caused by destructive interferences;

iii) Constructive interference smoothing: to eliminate the remaining extreme bright single pixels due to constructive interferences a 3 pixel-radius median filter is applied;

iV) Anisotropic diffusion filter: a selective filter to smooth the image.

3.2 Real Data Acquisition

The experimental setup used is presented in figure 3.11 [10]. Data was collected using an ultrasound scanner (SonixMDP, Ultrasonix) sampling at a frequency of 40 MHz. The transducer, a linear one, was operated at 10 MHz. The medium temperature was varied from approximately 37° to 41° C by using a water heating bath. The system circulates water through a copper pipe enabling sample heating. The temperature was measured using a J-type thermocouple connected to a digital multimeter (34972A, Agilent) 3.11.

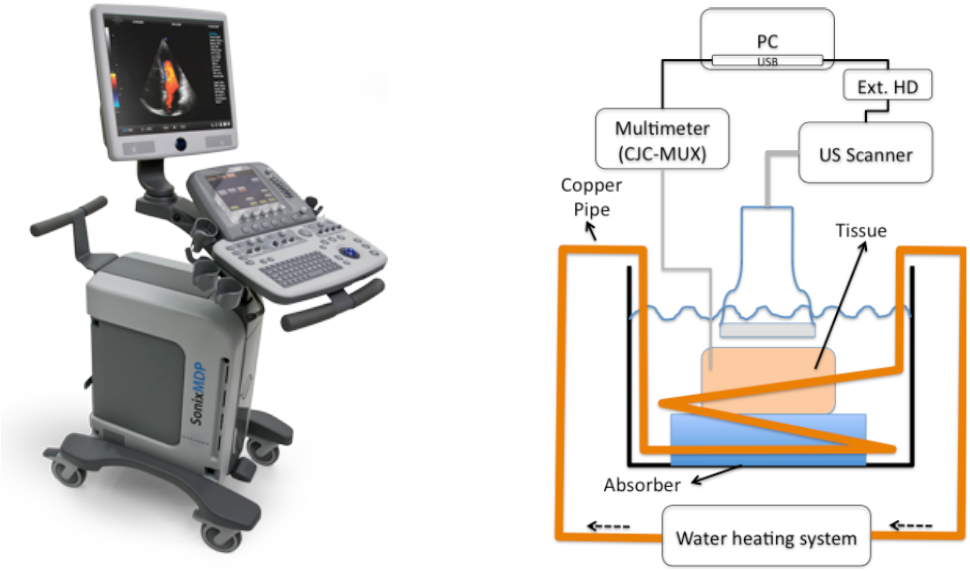

Figure 3.11: A) *SonixMDP ultrasound scanner.* **B)** *Experimental setup: samples are placed in a water bath that is heated by circulating water in copper pipes. Transducer is fixed in the apparatus top.*

3.2.1 Raw RF acquisition

Instead of saving the final B-mode images the raw RF signals were stored in a `.rf` file. To read the `.rf` file format a MATLAB script developed by *Corina Leung* was used [42]. The experiments were carried out using porcine fat and muscle shown in figure 3.12.A and 3.12.B, respectively. These samples were wrapped in a PVC film to avoid that water entered the samples and also to avoid outgassing, a problem referred in literature that consists in the release of gas that was dissolved in the medium. In what concerns the post-processing steps, cross-correlation between signals acquired at a given temperature and the signals obtained at a basal temperature was applied to correct for the echo-shifting due to the variations in sound speed [39]. Signals were then truncated in order to select only the echoes originated within the tissue samples. This was possible because the samples thickness and distance to the transducer were measure so we could use the echo ranging formulation and select the intended depth window. Finally energy of signals were calculated using (3.4) and normalized to the backscattered energy received at 37°C, as stated in (3.5). In fact CBE calculation was done using the same steps applied to the simulated data (section 3.1.7).

3.2.2 B-Mode acquisitions

Using the same experimental setup, presented in figure 3.11.B, B-mode images were acquired. Images were saved as a video with 25 frames-per-second. Experiment was carried out using an 4% agar-agar phantom containing two small pieces of muscle and porcine fat (figure 3.12.C) contrary to what was done in the raw RF acquisitions in each isolated tissues samples were used (figure 3.12.A and 3.12.B). Here, agar works as a scaffold to support our tissues pieces. Agar was used because it as acoustic properties similar to biological tissues and also because, due to its polymerization process, allows the insertion of the *ex-vivo* tissue samples at temperatures lower than 50°C, i.e, without damaging the tissue samples. The acquired video (each frame is a B-mode image) was then averaged in 5 seconds windows. This averaging step is done to eliminate possible artifacts (works as a low pass filter) [10]. Speckle

was reduced using the same method as in the simulated data, i.e, the algorithm developed by *Preetha et all* [41].

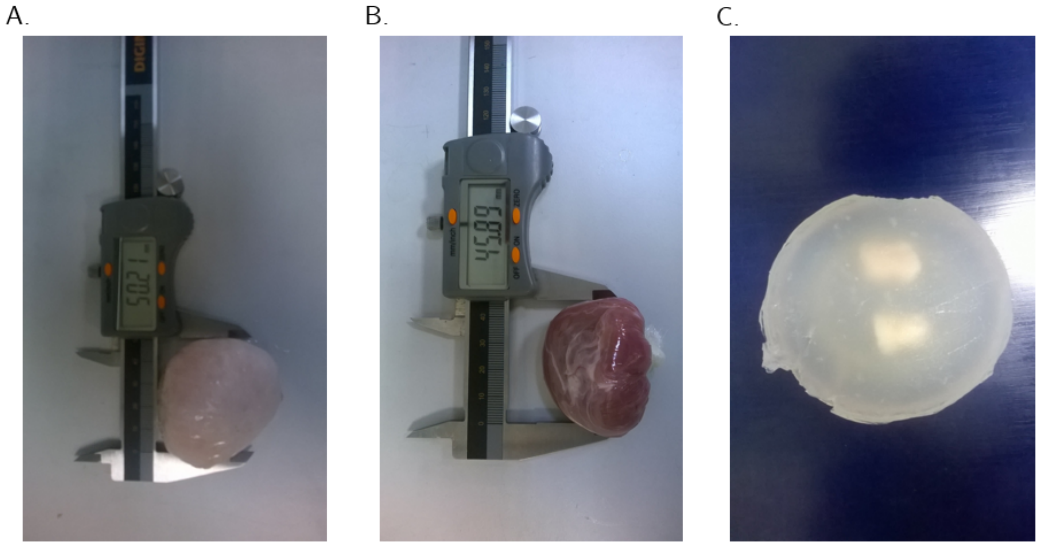

Figure 3.12: A) *Ex-vivo porcine fat sample*; **B)** *Ex-vivo porcine muscle sample. Both samples were wraped in a PCV film to avid outgassing.* **C)** *Phantom of 4% Agar-Agar, containing one piece of porcine muscle and one of fat.*

As being said, changes in sound speed when increasing the temperature causes the echoes to be shifted from the real position. Although this was not particular visible in simulated data, in real data this effect is largely visible. In fact, compensate images for apparent movement has been the focus of multiple works on this area [39]. If shifting occurs and is not corrected we can commit the mistake of comparing different regions in two images when the objective is to observe the intensity variation in the same region. Because the method applied previously in the raw RF signals may not be suitable for images (because is rigid), registration of images acquired at different temperatures was applied (non-rigid method) using the algorithm developed by *Kroon and Slump* [43] (see figure 3.13). In its core this method uses gradient maps to compute the adequate shift to each pixel.

Finally, as done for the simulated B-mode images, a polynomial fit to the pixel intensity variation is applied (see figure 3.10) [10]. Furthermore, it was computed the mean gray-level change of windows placed in different regions.

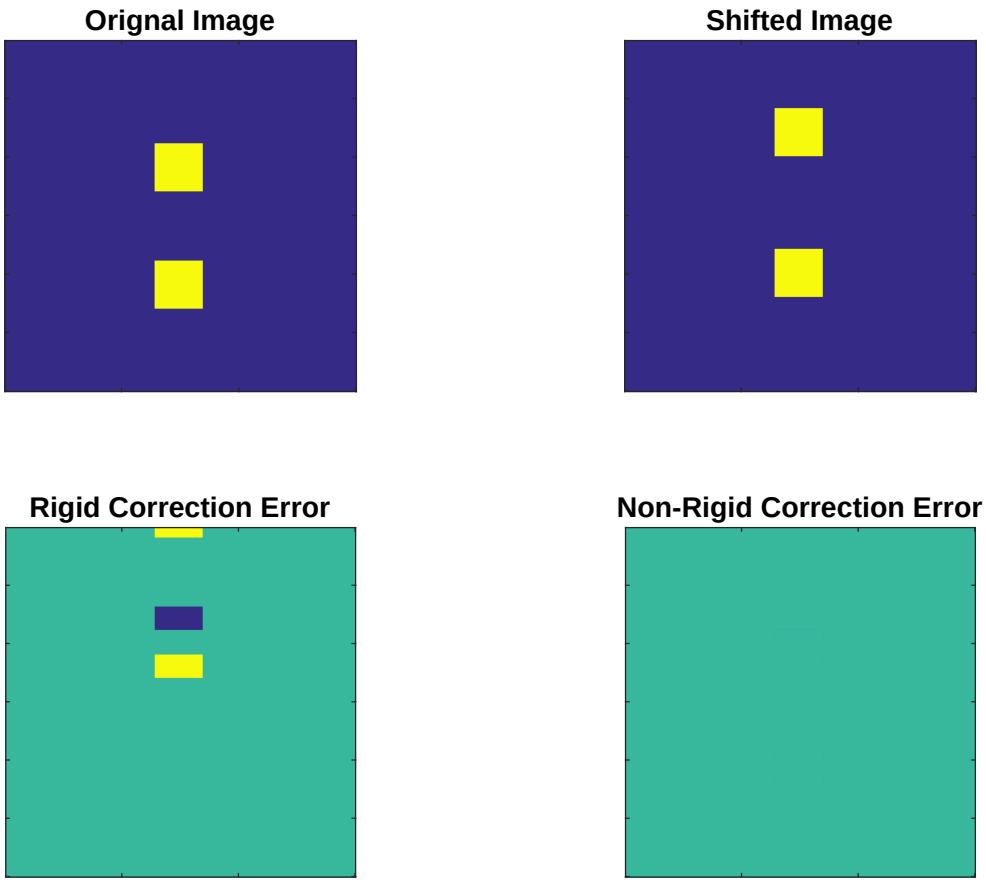

Figure 3.13: *Test and comparison of two shifting correction methods: a rigid an non-rigid method. As we can see rigid correction does not behave well if different shift values occur. In other hand the chosen non-rigid algorithm apparently shown a good response.*

4

Results and Discussion

In this chapter we first introduce the results obtained with the simulatations, followed by the attained with ex-vivo acquisitions. Their proceeding discussions are also performed in this chapter.

4.1 Simulated Data

4.1.1 A - scan signals

In figure 4.1.A it is an example of a RF signal obtained in a A-scan simulation. Applying the processing steps described in section 3.1.5, it is possible to visualize the echo envelope originated in the scattering region (figure 4.1.B). Using the echo-ranging formulation, the water sound speed (background medium) and taking into account that the scattering region extends from 10 to 18 mm away from the source, we can affirm that the backscattered signals are in the expected place as seen in figure 4.1 (approximately from 1.31 to 2.35 μs). This signal was obtained at a medium temperature of 37 °C. As the sound speed of the water increases with temperature, it was expected to see a shifting of the backscattered signals to the left (towards the source) when increasing the temperature. As expected this become visible as can be seen in figure 4.2. However, shifting does not show to be a problem in the analysis of A-scan signals because backscattered energy was calculated globally and not locally.

As has been said previously, monotonic changes in the envelope of this signal are expected to be detected when temperature increases, due to, almost exclusively, the sound speed temperature dependence. To assure that this is generally true, i.e., to guarantee that the distinct patterns of CBE are preserved for both types of scatterers in numerous conditions, multiples simulations were accomplished in which other variables were varied.

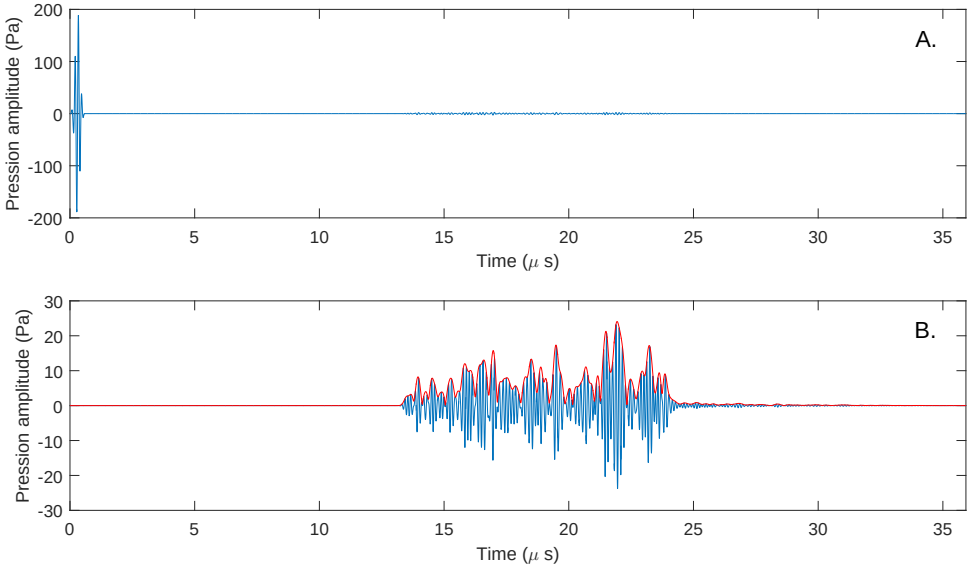

Figure 4.1: A) *Raw RF signal obtained in an A - scan simulation. The emitted burst is visible: a 4 cycle burst with a 5 MHz frequency was used to irradiate a region of fat scatterers. Due to the sub wavelength nature of the scatterers amplitude of the echoes are small.* **B)** *Detail of the backscattered echo signals originated in the scatterers.*

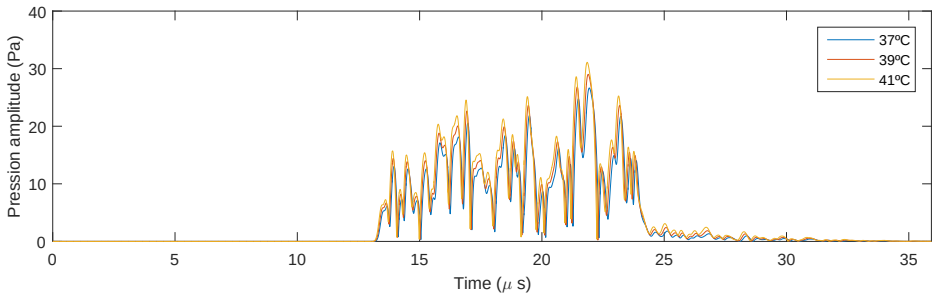

Figure 4.2: *Backscattered signals envelope from fat scatterers (ρ = 940kg/m^3) for a temperature of 37° C, 39° C and 41° C. A left shifting of the signals can be seen as expected due to the water sound speed positive variation. An amplitude increase with temperature of the signal envelope is also notable.*

Frequency dependence

Using a phantom in which the scattering region was filled with lipid scatterers ($\rho =$ 940 kg/m^3, A - scan signals were computed. Pulse frequency was varied from 1 to 9 MHz and temperature set to 37 °C. Figure 4.3 shows the backscattered energy obtained for each frequency at 37 °C. Increasing the pulse frequency, the received backscattered energy increased as well. In fact, after applying a fitting of multiple orders, we conclude that a 4^{th} order polynomial (Figure 4.3.B) enables a fitting with the smaller SSE (sum of squared errors), as expected by equation 2.9, that also states a fourth power frequency dependence for *Rayleigh* scattering. Similar results were obtained with aqueous scatterers ($\rho = 1040$ kg/m^3) instead of lipid ones.

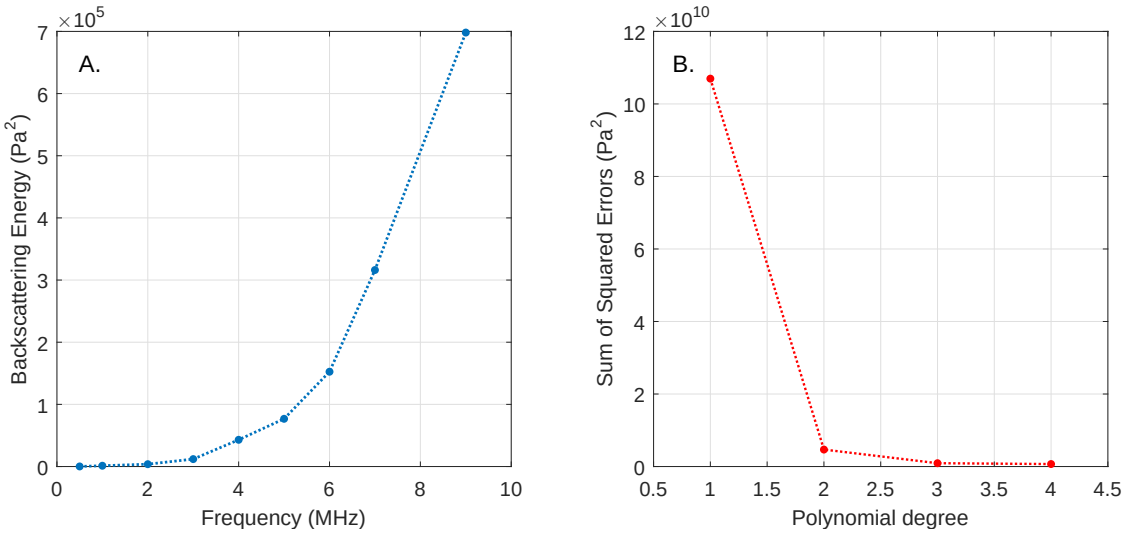

Figure 4.3: A) *Backscattered energy for multiple frequencies at 37° C.* **B)** *Sum of squared errors obtained with a polynomial fitting of 1^{st},2^{nd},3^{rd} and 4^{th} order.*

These simulations were repeated for multiple temperatures and for frequencies between 1 and 4 MHz. The resulting backscattered energy curves are then plotted for both lipid (figure 4.4.B) and aqueous scattering phantom (Figure 4.4.A). Normalizing the backscattered energy to the energy received at the initial temperature (37°C) we obtain the results shown in figure 4.5. CBE curves mantain their distinct monotonic increase and decrease for lipid and aqueous scatterers, respectively. In fact, at 41°C, the difference between curves simulated with different frequencies is less than 0.25 dB for both scattering media.

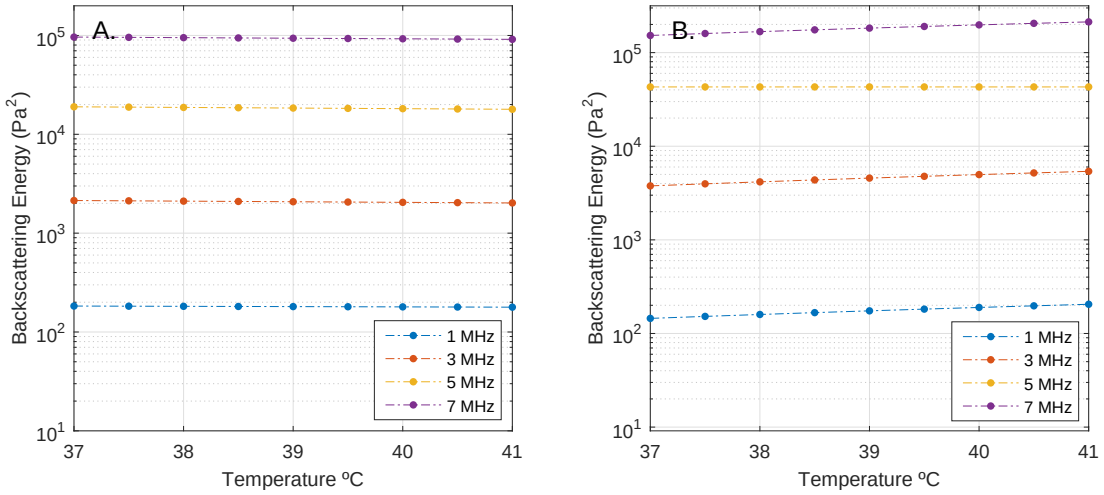

Figure 4.4: **A)** *Backscattered energy variation along temperature for multiple frequencies for a phantom containing a region of aqueous scatterers (ρ = 1040 kg/m^3).* **B)** *Backscattered energy variation along temperature for multiple frequencies for a phantom containing a region of fat scatterers (ρ = 940 kg/m^3).*

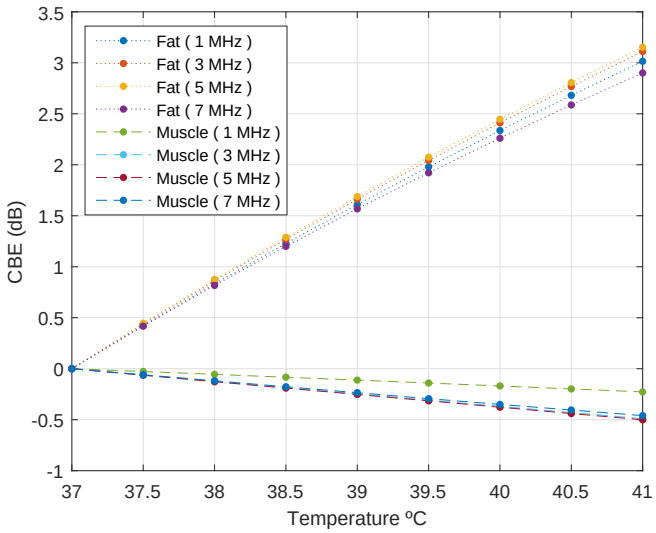

Figure 4.5: *CBE curves for multiple frequencies for both lipid (dotted line) and aqueous, or muscle, scattering media (dashed lines).*

Scatterers concentration

Due to the importance of medium scatterers distribution in the statistics of the backscattered signals, several simulations were designed to test the importance of scatterers concentration, i.e., the number of scatterers per mm^2. In equation (2.18)

it was taken the assumption that power received by a number of scatterers is proportional to the one received by only one, statement that we were also able to verify from our simulated data, using a pulse frequency of 7.5 MHz (as used in *Straube et al* studies) as can be seen in figure 4.6.A. The number of scatterers per mm^2 does not seem to have a major influence in the normalized backscattered energy curves of aqueous scattering medium (Figure 4.6.B). For the lipid scattering medium difference between the curve acquired with different scatterers concentration is bigger (figure 4.6.B). However they all show a distinct growing monotonous behavior as expected for lipid scatterers.

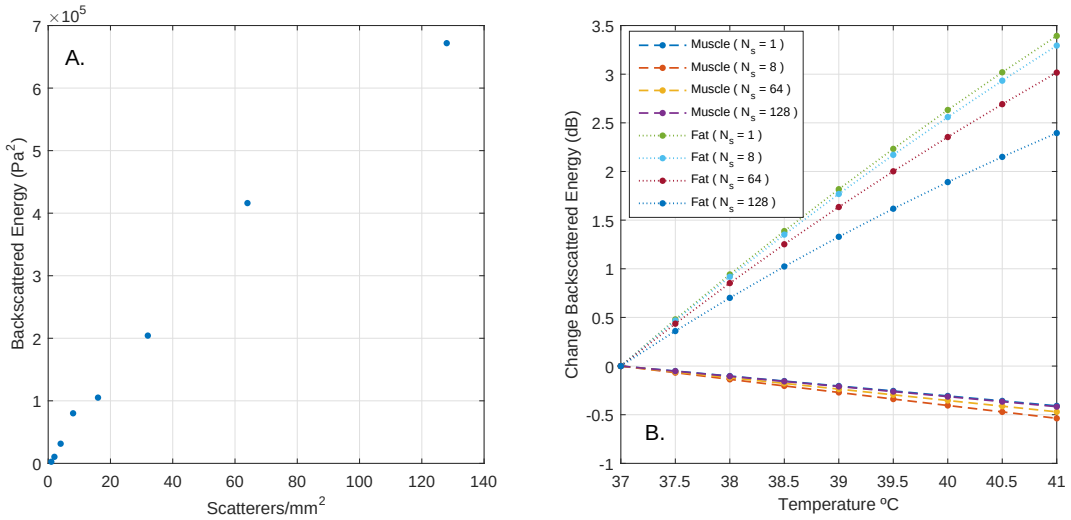

Figure 4.6: **A)** *Backscattered energy variation with the increasing number of scatterers/mm^2 for a phantom containing a region of lipid scatterers (ρ = 940 kg/m^3).* **B)** *CBE curves along temperature for a different number of scatterers distributions. Lipid scattering medium (ρ = 940 kg/m^3) represented by the dotted lines and aqueous scattering medium (ρ = 1040 kg/m^3).*

Scatterers Density

Lastly, are presented the results of simulations in which the density of scatterers was varied. Three different densities were chosen within the range presented in table 3.2. Due to the impedance mismatch to the water background, regardless of the density chosen, signals amplitude from fat were always higher that the received from the muscle scatters. In what concerns the CBE, a maximum difference of 1.2 dB can be observed between the curves of lipid scattering medium at 41°C (figure 4.7). The

aqueous (or muscle) scattering medium showed a difference of less than 0.25 dB between the three CBE curves at 41°C.

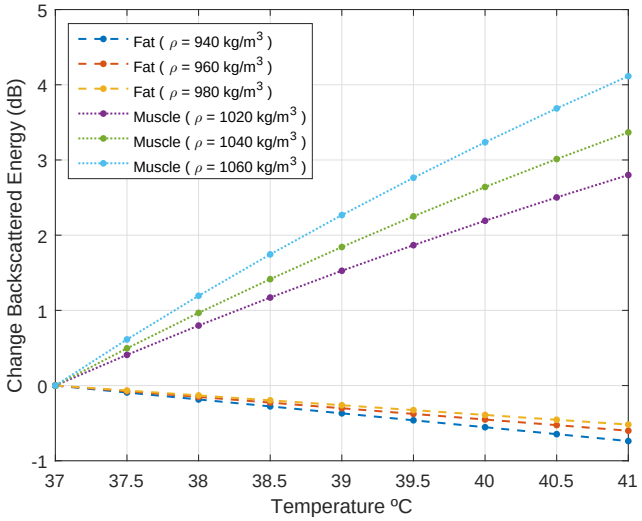

Figure 4.7: *CBE curves for both fat and muscle scattering media.*

These results show that the primarily difference of the CBE curves are caused by the differences in sound speed of both the scatterers and the medium. None of this 3 studied variables caused significant changes in the CBE curves to the point of destroying the clear distinct signatures of the two types of scatterers. In all simulations aqueous scattering media show monotonic decreasing CBE curves unlike the lipid scattering medium that show a clear crescent monotonic CBE curve.

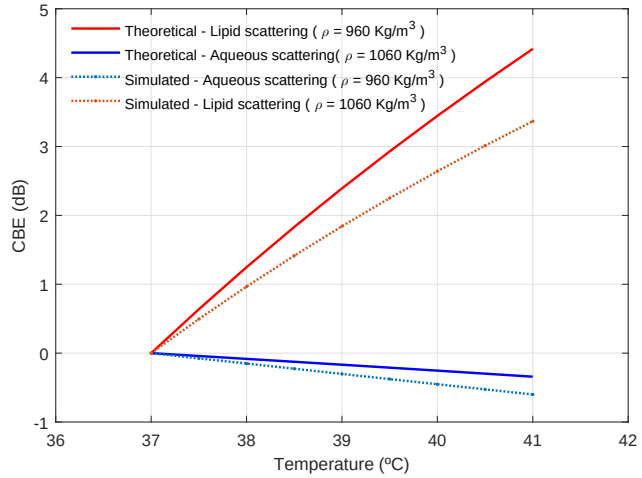

Figure 4.8: *Comparison of simulated CBE (dashed lines) with the theoretical model (continuous lines) for both lipid (red lines) and muscle scatterers (blue lines) in a water background.*

4.1.2 B - mode Images

In figure 4.9 it is presented the B-mode image obtained for the simulation described in section 3.1.8, at a basal temperature (37°C). As is possible to observe, image contains the traditional speckle presented in real ultrasound images. Taking into account the different scattering regions designed (see figure 3.9) we can say that is very difficult to distinguish them in a conventional B-mode image due to the low contrast between the different regions of interest.

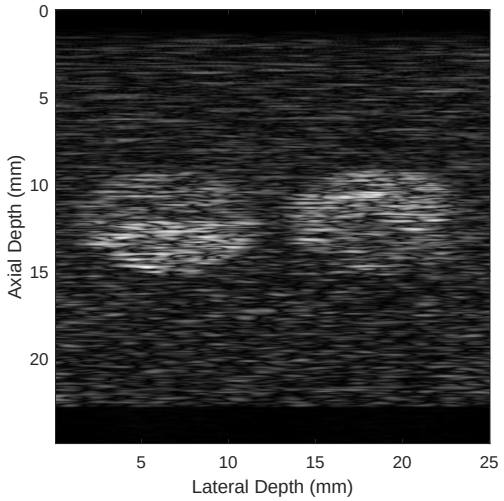

Figure 4.9: *Simulated conventional B-mode image obtained using the phantom presented in figure 3.8*

Considering the volume of 7 images simulated in the temperature range between 37°C and 40°C, speckle was reduced to decrease its influence in the tracking of CBE along temperature (algorithm presented in section 3.1.8). In figure 4.10 is shown the B-mode image with softened speckle. It is possible to observe the typical blurring effects characteristic of this type of algorithms (due to use of multiple median filters). Using images with softened speckle, the mean gray level in four windows, one in each region of interest, was tracked and normalized to the gray level at 37°C (graphic 4.10.B). For the windows located in the lipid scattering regions (red squares) we can see a monotonic crescent curve for the gray level intensity. Although the magnitude of the changes (1.4 dB) is lower than expected by theoretical model (3.2 dB at 40°C), their behavior is as expected. This magnitude difference may be due to the

speckle itself or the algorithm to reduce it. Regarding the aqueous scattering regions different behavior was observed depending on the relative position of the different scattering media. This lead to the conclusion that the CBE of a scattering medium could be potentially influenced by the media located *a priori*, because the beam power that reaches a region may not be the same for every temperature.

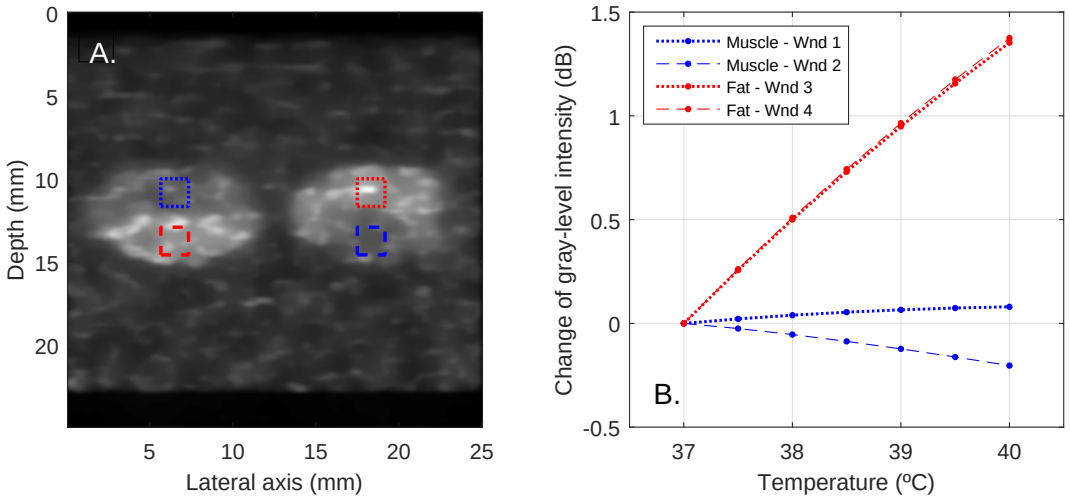

Figure 4.10: **A)** *Conventional B-Mode with reduced speckle. 4 windows (Wnd) are considered: two in the region of aqueous (blue squares) and two in the region of lipid scatterers (red squares).* **B)** *Change in the gray level of the windows considered.*

A linear fit to the gray-level variation of each pixel was then applied. Map of the linear coefficient for each pixel are presented in figure 4.11.A. As can be observed it is possible to identify the lipid scattering regions but the aqueous (or muscle) scattering regions are not totally identifiable. Analyzing the histogram distribution of the linear fitting values (Figure 4.12), coefficients for lipid regions show a peak at approximately 0.7 dB, unlike the aqueous regions that show a peak at about - 0.05 dB, i.e., close of zero (mainly the background value). However lipid scattering regions show another peak at about 0.05 dB as well. We were unable to hypothesis the reason of this bi-modal distribution. It can be observed that the fitting coefficients for pixels located in the lipid regions are much higher than the values for muscle scattering regions. This could caused the stretching of color map making the coefficients of muscle regions hard to visualize in the map (figure 4.11). Therefore, in a final approach we normalize each B-mode image, between 0 and 1, before applying the

pixel fitting. Resulting fitting maps were considerable better for both linear and quadratic coefficients (4.11.B).

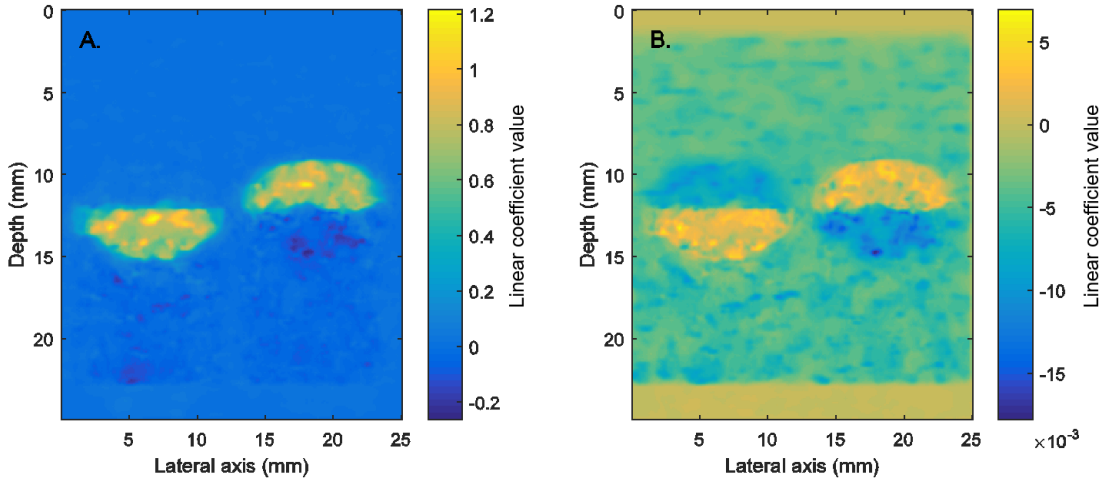

Figure 4.11: **A)** *Linear fit coefficients map of the pixels intensities variations with temperature.* **B)** *Linear fit coefficients map using normalize B-mode images.*

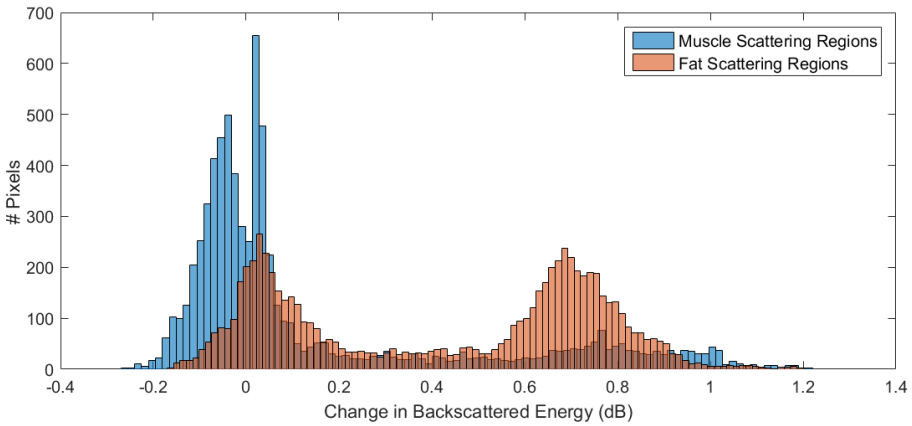

Figure 4.12: *Histogram of linear fit coefficients for both the lipid and aqueous scattering regions.*

To conclude our work with simulated data, and aiming to evaluate the ability to classify different tissues non-invasively, we tested a simple computational segmentation and classification of the linear fitting coefficients map using *Otsu* segmentation (`multithresh` matlab function). This technique find multiple thresholds that minimize the intra-class variance. In our case two thresholds are selected in order to generate 3 classes: lipid and aqueous scattering regions, and background, as presented in figure 4.13.B (yellow represent lipid scatterers regions, deep blue aqueous

scatterers regions and soft blue background). This segmented image can be overlayed with the conventional B-Mode image resulting in the image of figure 4.14.

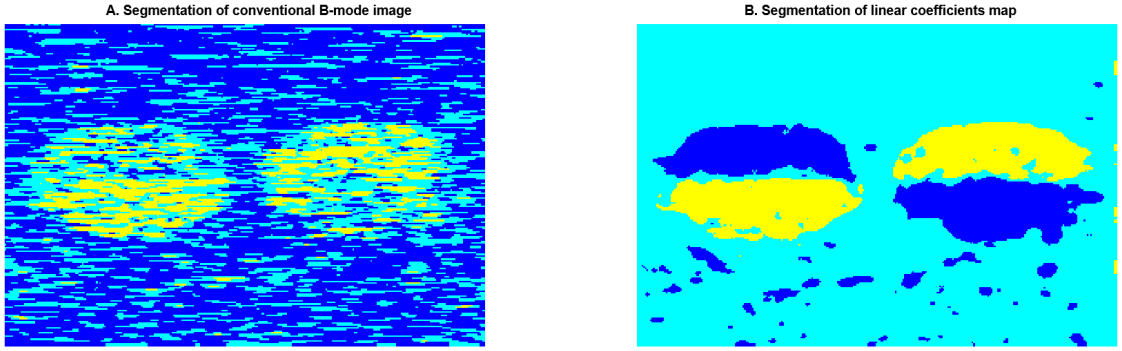

Figure 4.13: **A)** *Segmentation of the conventional B-Mode image using Otsu method.* **B)** *Segmentation results of the linear fit map using Otsu method.*

The results with simulated B-mode images, lead us to conclude that although the new image show a small blurring it contains more information and image detail about the media that can not be extracted from the conventional B-mode image: it is possible to look at the obtained parametric image and conclude that bottom and top of the left and right disk regions, respectively, have a complete different nature of the other two regions (top and bottom of the left and right disk regions respectively). We were able to segment lipid scattering regions (fat) with a accuracy of 89% and aqueous scattering regions (muscle) with accuracy of 87%. This values were calculated using the target masks presented in figure 3.9.

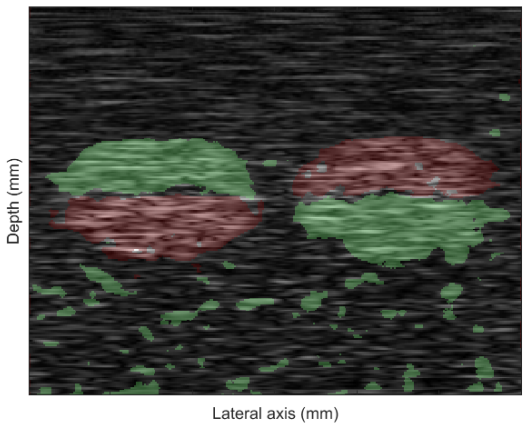

Figure 4.14: *Overlay of conventional B-mode image, presented in 4.9.A, and the image resulting from the segmentation of the linear fit map presented in 4.13.B*

4.2 Ex-vivo data

4.2.1 Raw RF acquisition

The ultrasound scanner used in experimental setup returns 256 RF lines for each sample. In figure 4.15 is shown one of the RF scan lines (150^{th} line) acquired. Signals were truncated to assure that the backscattering energy calculated is only from echoes from within the tissue samples (regions of interest - ROIs).

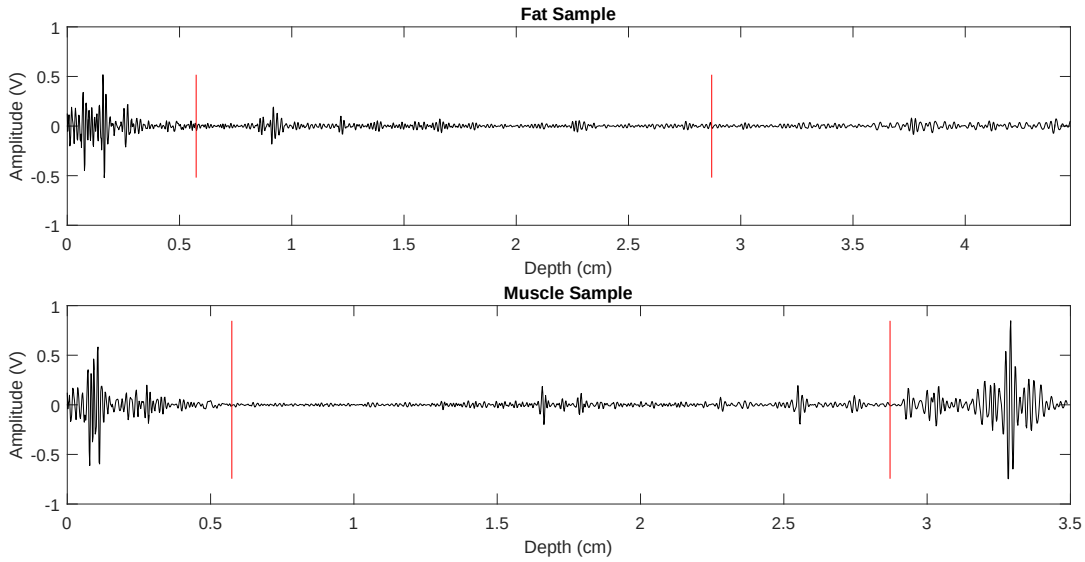

Figure 4.15: *RF signal of a scan line from fat sample (at top) and muscle sample (at bottom). Red lines delimit the truncated zone to select only echoes from within the sample.*

In figure 4.16 the evolution with temperature of the backscattered signals in ROIs are presented. As expected and reported in other studies, echo shifting is present: increasing the temperature, echoes shift slightly to the right. Consulting sound speed curves present in figure 3.6, it was expected a right shift from fat echoes and a left shift from muscle echoes. However, due to the presence of water between the transducer and samples we expected the shift to be slightly unpredictable, and we also suspected that this shift was also due to sample movement during acquisition rather than only sound speed changes because sometimes it was observed oscillations in signals when small movements occurred in the experimental bench. Before

selecting the ROIs and proceed to the CBE analysis it was corrected the shifting with a cross-correlation approach (Figure 4.17) to ensure that we are analyzing the same backscattering echoes for all temperatures.

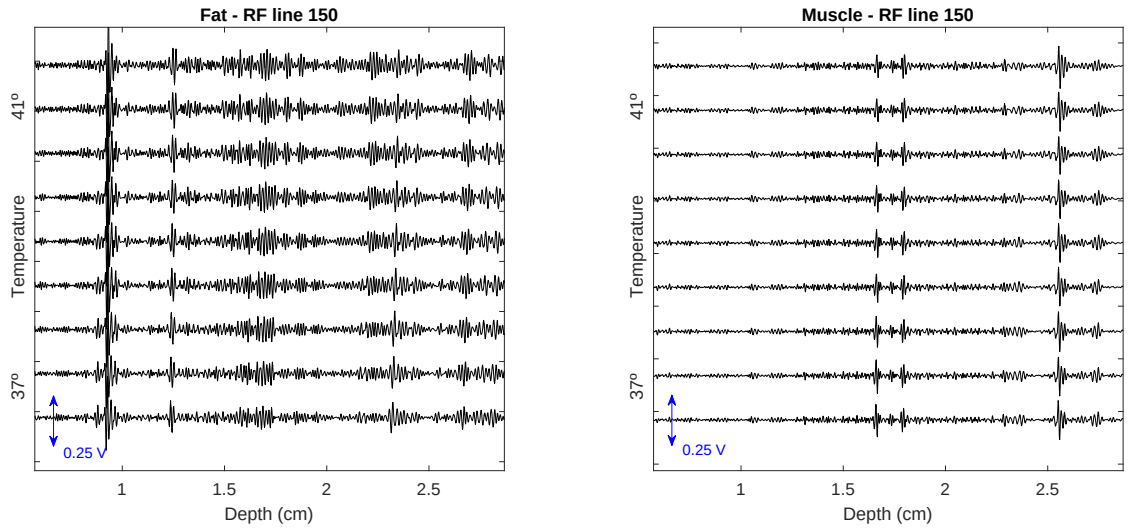

Figure 4.16: *ROIs evolution with temperature for fat (at left) and muscle sample(at right). Shifting is visible in both samples.*

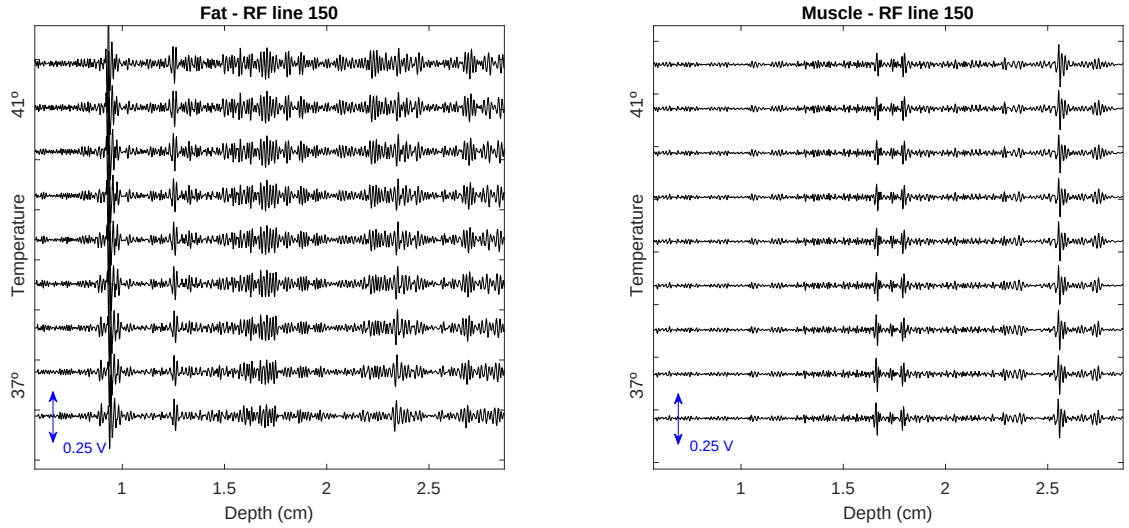

Figure 4.17: *ROIs evolution with temperature for fat (at left) and muscle sample(at right) corrected for the apparent shifting with a cross-correlation method. A change in echoes amplitude with temperature is already notable.*

CBE curves for each of the RF signals was computed using (3.4) and (3.5). It is evident that the change in backscattered energy when increasing temperature

from 37 to 41°C is distinct for the two samples. For the fat sample, a change in average of 3.3 ± 3 dB can be reported between the backscattered energy received at 37°C and 41°C (Figure 4.18.A). In other hand, in muscle sample this change is in the order of 0.3 ± 2.4 dB (Figure 4.18.A). It is fair to assume that the curves are distinct for each sample (Figure 4.18.B). However to statistically prove it, a *Kruskal-Wallis* was applied to test if they are indeed distinct. We attained a *p-value* of $5.8294\text{x}10^{-253}$, i.e., approximately 0. This being said, and as the *p-value* obtained is smaller than 0.05, we can conclude about the distinct nature of CBE distributions from fat and muscle samples. Furthermore mean CBE changes, mostly from fat sample, approximate from the expected values of theoretical model (4.8).

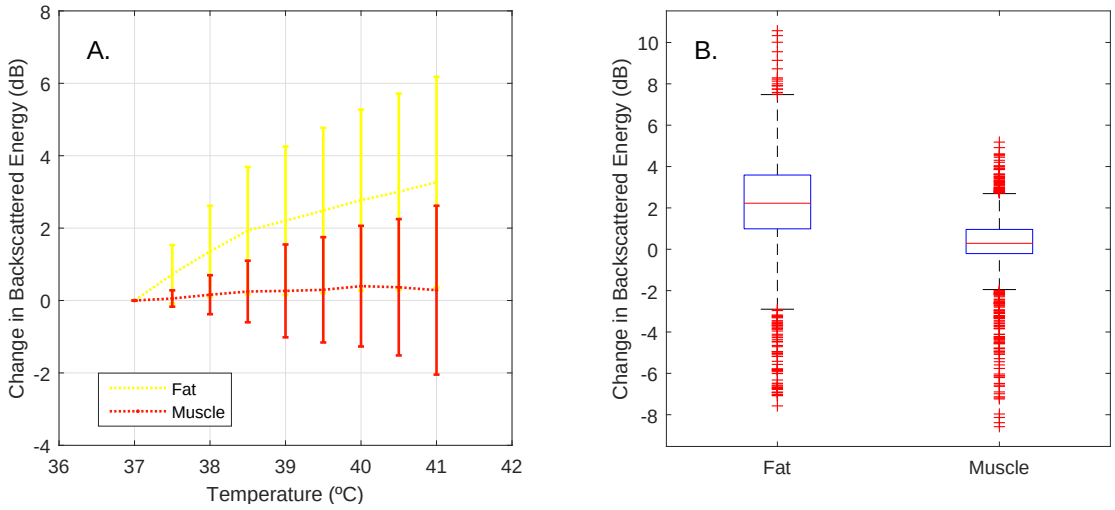

Figure 4.18: **A** *Average CBE curves calculated from all the RF signals for muscle sample (red line) and for fat sample (yellow line).* **B** *Box plot of the CBE values for both the fat and muscle samples. A p-value of 5.8294e-253 was attained using a Kruskal-Wallis test.*

4.2.2 B-mode images acquisition

Concerning the results obtained in the B-Mode acquisitions in *ex-vivo* tissues, in figure 4.19 is presented the image acquired at the basal temperature ($\sim$ 37°C). It is possible to identify the two major pieces of ex-vivo tissue placed in the agar medium: at the left porcine muscle piece, and at the right the porcine fat piece. The total depth of the phantom is 2 centimeters.

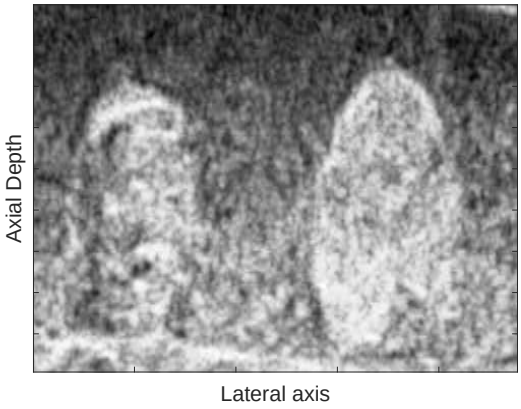

Figure 4.19: *Conventional B-mode of the agar phantom containing porcine muscle (left structure) and fat (right structure) ex-vivo samples.*

Gray level intensity was tracked for three distinct windows: a window containing all image, a window within the muscle region and a window within the fat region, as presented in figure 4.20.A. As we can see by the normalized curves presented in graphic of figure 4.20.B the regions show a distinct evolution in gray level with temperature. At 41°C, gray level increased approximately 0.07 dB for the window containing fat and decreased approximately 0.05 dB in the window containing muscle (comparing to the gray level obtained at initial temperature, i.e., 37 °C). However these curves do not show a monotonic behavior as expected by the theoretical models and obtained with simulated data. Furthermore magnitude of changes is very small. This may be due to several problems as undesired movements in the experimental setup or even due to a bad planing and construction of the agar phantom.

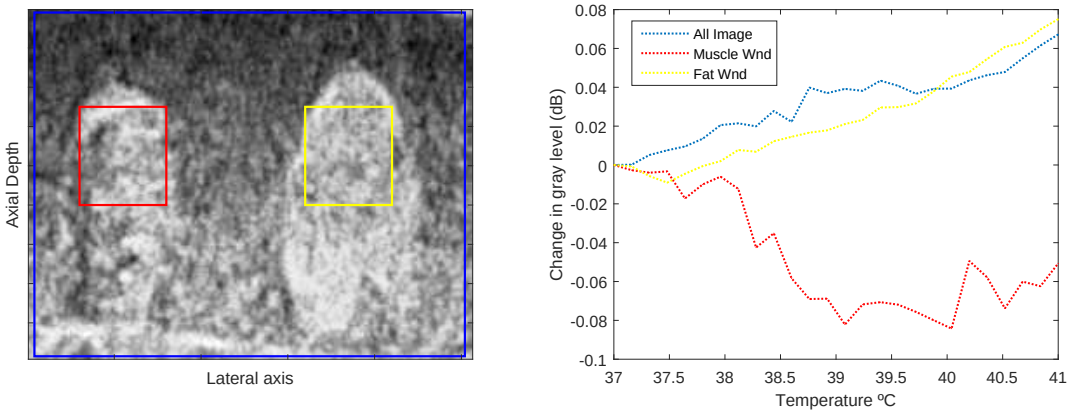

Figure 4.20: **A)** *Conventional B-Mode image. Three windows were considered: one containing all image (blue window), and 30x30 pixel windows within muscle (blue window) and fat region (yellow window).***B)** *CBE curves for the 3 described windows.*

After applying the same method followed in the simulated images, i.e, reduction of the speckle and normalization of the images, the registration algorithm presented in section 3.2.2 was applied. It is difficult to quantify the effectiveness of shifting correction because our technique aims itself to change in gray level intensity between images. Furthermore, we were not sure if the algorithm changed itself the pixels gray level intensities. This being said, we believed that the registration algorithm was a better approach than a rigid correction of the images (or no correction at all). A linear polynomial fit was applied to each pixel. The coefficients of this fit are presented in figure 4.21.A. The *Otsu* method was also tested to segment the linear coefficients map resulting in the image presented in 4.21.B. As we can see in this two images, results were not good as the two different tissues are difficult to identify in the fitting map. Consequently, segmented image does show good results as well. Different segmentation methods should have been tested but it was impossible due to time issues. One problem that may weaken the results was the fact that agar phantom was very permeable and during the 30 minutes acquisition, water content within the polymeric phantom increased as observed by the differences in rigidity before and after the acquisitions. This may have caused *outgassing* of the biological tissue samples and their faster degradation. Excessive gain on acquisition may also have been a problem.

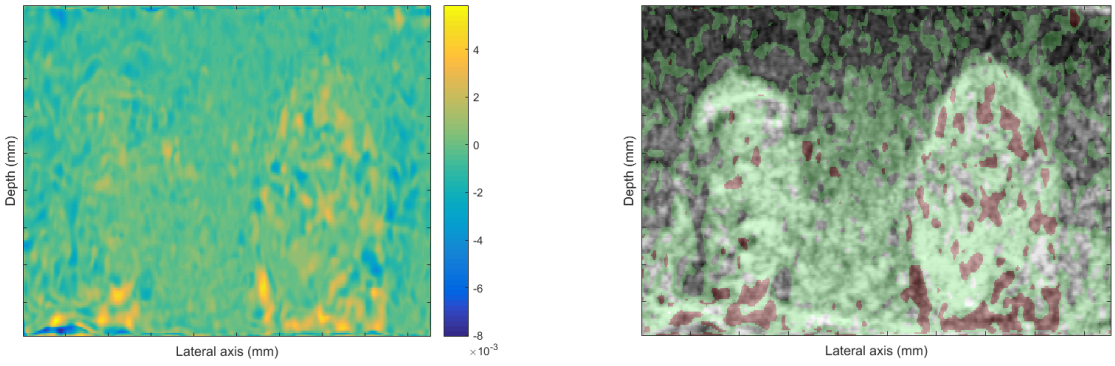

Figure 4.21: A) *Linear fit coefficients map.***B)** *Segmentation of linear fit coefficients map using Otsu method.*

5

Conclusions and Future Work

In this work it was tested the hypothesis of using temperature induced CBE for tissue assessment. To achieved this, we followed a double strategy composed by analysis of both simulated and real data. Therefore, we can say that the main objective of this thesis was achieved, i.e, we were able, in a computational simulated environment, to induce and track changes in backscattered energy using temperature and build a new map that enhance the differences in temperature response of distinct scattering media. At this level, in a future work, simulations should be improved and get closer to real tissue cases, i.e, more diversity in the scatterers type and cross-sections. Concerning the acquisitions in real data, although promising results were achieved using RF signals from isolated tissue samples, in which totally different CBE curves were observed for muscle and fat samples, using a agar phantom containing two different tissue types (fat and muscle) only small differences were attained. In fact the linear coefficients mapping did not reveal any useful information, and we put the hypothesis that this was due to a excessive gain in image acquisitions. Future work should encompass the minimization of undesired movement in the experimental setup and also by a better characterization of the echo-shifting and the correspondent correction algorithms. Concluding we think that CBE seem to be a robust and promising feature for non-invasive tissue classification. Envisaging a real-world application in-vivo, precise and local heating capabilities offered by HIFU technology (heating up to 4°C) could give a response in how to heat and induced CBE, leading to real repercussions in medical imaging. Of course, application *in-vivo* in humans would need a serious evaluation of the risk-benefits of the methodology.

Bibliography

[1] T. L. Szabo, *Diagnostic Ultrasound Imaging: Inside Out*. Elsevier, 2013.

[2] R. Simões, "Thermo-responsive ultrasound imaging: modeling and preliminary results," 2014. Biomedical Engineering MsC Thesis.

[3] R. Sabbagha, *Diagnostic Ultrasound: Applied to Obstetrics and Gynecology*. Lippincott, 1987.

[4] Asbjørn Støylen, "Basic ultrasound, echocardiography and doppler for clinicians," 2013. Retrieved from `http://folk.ntnu.no/stoylen/strainrate/new.html` at 2016-09-11.

[5] C. N. D. Course, "Controlo não destrutivo por ultra-sons." Retrieved from `http://ltmeu.deec.uc.pt/wp-content/uploads/2012/07/CND1.pdf` at 2016-04-03.

[6] F. W. Kremkau and F. Forsberg, *Sonography principles and instruments*. Elsevier Health Sciences, 2015.

[7] J. Kennedy, G. Ter Haar, and D. Cranston, "High intensity focused ultrasound: surgery of the future?," *The British journal of radiology*, 2014.

[8] W. Straube and R. M. Arthur, "Theoretical estimation of the temperature dependence of backscattered ultrasonic power for noninvasive thermometry," *Ultrasound in medicine & biology*, vol. 20, no. 9, pp. 915–922, 1994.

[9] B. Treeby, B. Cox, and J. Jaros, *k-Wave: A MATLAB toolbox for the time domain simulation of acoustic wave fields*. 2012.

[10] C. A. Teixeira, A. Fontes, M. Von Kruger, A. V. Alvarenga, and C. W. Pereira, "Expressiveness of temperature-induced changes in backscattered energy in conventional b-mode images," in *Proceedings of Meetings on Acoustics*, vol. 19, p. 075006, Acoustical Society of America, 2013.

[11] Paul Kinahan, "Bioengineering 508: Physical aspects of medical imaging," 2006. Retrieved from `http://courses.washington.edu/bioen508/Lecture6-US.pdf` at 2016-09-11.

[12] H. Azhari, *Basics of biomedical ultrasound for engineers*. John Wiley and Sons, 2010.

[13] J. Park, J. B. Kang, J. H. Chang, and Y. Yoo, "Speckle reduction techniques in medical ultrasound imaging," *Biomedical Engineering Letters*, vol. 4, no. 1, pp. 32–40, 2014.

[14] F. Tranquart, N. Grenier, V. Eder, and L. Pourcelot, "Clinical use of ultrasound tissue harmonic imaging," *Ultrasound in medicine & biology*, vol. 25, no. 6, pp. 889–894, 1999.

[15] J.-L. Gennisson, T. Deffieux, M. Fink, and M. Tanter, "Ultrasound elastography: principles and techniques," *Diagnostic and interventional imaging*, vol. 94, no. 5, pp. 487–495, 2013.

[16] C. R. Merritt, "Doppler color flow imaging," *Journal of clinical ultrasound*, vol. 15, no. 9, pp. 591–597, 1987.

[17] R. M. Arthur, W. L. Straube, J. D. Starman, and E. G. Moros, "Noninvasive temperature estimation based on the energy of backscattered ultrasound," *Medical physics*, vol. 30, no. 6, pp. 1021–1029, 2003.

[18] H. Lutz and E. Buscarini, *Manual of diagnostic ultrasound*, vol. 2. World Health Organization, 2013.

[19] W. Hedrick, L. Hykes, and E. Starchman, *Ultrasound Physics and Instrumentation*. Mosby, 1992.

[20] B. Cox, *Acoustics for Ultrasound Imaging*. 2013.

[21] P. Laugier and G. Haïat, *Bone Quantitative Ultrasound*. Springer, 2011.

[22] G. Leon Van Der, "Frequency- and angle dependency of the scattering of ultrasound as a contrast mechanism for imaging blood in the neonatal brain," 2015.

[23] H. Jakjoud, A. Chitnalah, N. Aouzale, and D. Caviglia, "Measurement of the nonlinear ultrasonic parameter in aqueous solutions," *Moroccan Journal of Condensed Matter*, vol. 12, no. 2, 2010.

[24] C. Multiphysics, "Piezoelectric effect." Retrieved from `https://www.comsol.pt/multiphysics/piezoelectric-effect` at 2016-09-12.

[25] A. Ng and J. Swanevelder, "Resolution in ultrasound imaging," *Continuing Education in Anaesthesia, Critical Care & Pain*, vol. 11, no. 5, pp. 186–192, 2011.

[26] N. Tole and H. Ostensen, *Basic physics of ultrasonographic imaging*. World Health Organization, 2005.

[27] P. Hoskins, K. Martin, and T. Abigail, *Diagnostic Ultrasound: Physics and Equipment*. Cambridge University Press, 2010.

[28] M. A. Morgan and A. G. et al., "Harmonic imaging." Retrieved from `http://radiopaedia.org/articles/harmonic-imaging` at 2016-09-12.

[29] D. L. Miller, N. B. Smith, M. R. Bailey, G. J. Czarnota, K. Hynynen, I. R. S. Makin, B. C. of the American Institute of Ultrasound in Medicine, *et al.*, "Overview of therapeutic ultrasound applications and safety considerations," *Journal of Ultrasound in Medicine*, vol. 31, no. 4, pp. 623–634, 2012.

[30] C. Speed, "Therapeutic ultrasound in soft tissue lesions," *Rheumatology*, vol. 40, no. 12, pp. 1331–1336, 2001.

[31] B. Billard, K. Hynynen, and R. Roemer, "Effects of physical parameters on high temperature ultrasound hyperthermia," *Ultrasound in medicine & biology*, vol. 16, no. 4, pp. 409–420, 1990.

[32] H. Shankar and P. S. Pagel, "Potential adverse ultrasound-related biological effectsa critical review," *The Journal of the American Society of Anesthesiologists*, vol. 115, no. 5, pp. 1109–1124, 2011.

[33] D. Dalecki, "Mechanical bioeffects of ultrasound," *Annu. Rev. Biomed. Eng.*, vol. 6, pp. 229–248, 2004.

[34] J. Ophir, "Estimation of the speed of ultrasound propagation in biological tissues: A beam-tracking method," pp. 359–368, 1986.

[35] R. A. Sigelmann and J. M. Reid, "Analysis and measurement of ultrasound backscattering from an ensemble of scatterers excited by sine-wave bursts," *The Journal of the Acoustical Society of America*, vol. 53, no. 5, pp. 1351–1355, 1973.

[36] B. E. Treeby and B. T. Cox, "k-wave: Matlab toolbox for the simulation and reconstruction of photoacoustic wave fields," *Journal of biomedical optics*, vol. 15, no. 2, pp. 021314–021314, 2010.

[37] J. A. Jensen, "Field: A program for simulating ultrasound systems," in *10TH NORDICBALTIC CONFERENCE ON BIOMEDICAL IMAGING, VOL. 4, SUPPLEMENT 1, PART 1: 351–353*, Citeseer, 1996.

[38] M. A. Morgan and A. G. et al., "Focus." Retrieved from `http://www.egr.msu.edu/~fultras-web/` at 2016-09-12.

[39] J. W. Trobaugh, R. M. Arthur, W. L. Straube, and E. G. Moros, "A simulation model for ultrasonic temperature imaging using change in backscattered energy," *Ultrasound in medicine & biology*, vol. 34, no. 2, pp. 289–298, 2008.

[40] X. Li, G. Ghoshal, R. J. Lavarello, and M. L. Oelze, "Exploring potential mechanisms responsible for observed changes of ultrasonic backscattered energy with temperature variations," *Medical physics*, vol. 41, no. 5, p. 052901, 2014.

[41] N. Preetha, T. Arthi, and M. Venkateswari, "Modified kernel anisotropic diffusion despeckle filter for medical ultrasound imaging,"

[42] C. Leung, "Rf reader," 2007. Retrieved from `http://research.ultrasonix.com/` at 2016-09-12.

[43] D.-J. Kroon and C. H. Slump, "Mri modalitiy transformation in demon registration," in *2009 IEEE International Symposium on Biomedical Imaging: From Nano to Macro*, pp. 963–966, IEEE, 2009.

Appendix

Proceeding Papers Published

ICA 2016 BUENOS AIRES
Buenos Aires – 5 to 9 September 2016
Acoustics for the 21st Century...

PROCEEDINGS of the 22nd International Congress on Acoustics

Physical Acoustics-Ultrasound: Paper 819

ON THE POSSIBILITY OF NON-INVASIVE TISSUE ASSESSMENT USING INDUCED CHANGES IN BACKSCATTERED ENERGY: A K-WAVE SIMULATION

André Pedrosa[(a)], Ricardo Simões[(a)], Marco von Kruger[(b)], André Alvarenga[(c)], Wagner Pereira[(b)], César Teixeira[(a)]

[(a)]University of Coimbra, Portugal, aes.pedrosa@gmail.com
[(b)]Biomedical Engineering Program - COPPE, Federal University of Rio de Janeiro, Brazil, wagner.coelho@ufrj.br
[(c)]INMETRO, Brazil

Abstract:

Ultrasound (US) propagation properties change with temperature. One US feature that was studied is the change in backscattered energy (CBE). Theoretical models and experiments have shown that different types of tissues, made of different scatterer types, when submitted to a temperature change can produce distinct CBE. Thus, given these distinct changes on CBE, one could raise the hypothesis that CBE could be also useful for non-invasive tissue assessment. In this study an ultrasound toolbox, k-Wave (`www.k-wave.org`) is used to simulate CBE for different tissue types and properties. The implemented geometry consists of a 2D geometry simulating a water medium. Two distinct highly scattering regions were designed within this aqueous medium: one region of lipid-based scatterers (simulating fat) and one region of water-based scatterers (simulating muscle). Backscattered signal profiles for temperatures within the range $37°C$ to $41°C$ were computed. The simulated US transducer was excited at $7.5MHz$. Amplitude variations of the RF signals were evaluated for the different temperatures by a linear fitting. As expected and shown by previous studies fat and muscle scatterers regions have shown a positive and negative variation, respectively. Our results show a positive variation of $0.7510dB°C^{-1}$ and a negative variation of $-0.1086dB°C^{-1}$, as seen in literature for fat with density of $950kgm^{-3}$ and muscle with density of $1065kgm^{-3}$, respectively. Changing muscle density to $1085kgm^{-3}$, the CBE variation was $-0.0948dB°C^{-1}$, and changing fat density to $920kgm^{-3}$, the CBE value increases in a rate of $0.7510dB°C^{-1}$. The developed simulation reinforces that idea that CBE could be valuable for non-invasive tissue classification. Future studies will include the validation of the simulation with data collected from laboratory experiments.

Keywords: Ultrasound, CBE, Simulation

On the possibility of non-invasive tissue assessment using induced changes in backscattered energy: a k-wave simulation

1 Introduction

Ultrasound has shown to be a versatile, non-invasive and low-cost medical imaging technique as well as a therapeutic solution [8]. However, its image quality is lower than those achieved by other techniques, such as magnetic resonance imaging (MRI) [7]. This fact has lead to the appearance of multiple ultrasound-based methodologies in order to combine the advantages of ultrasound with a improved imaging quality, and that in an ideal situation could enable non-invasive tissue assessment, i.e., the attainment of quantitative ultrasound (QUS) capabilities. One example is elastography that explores the elastic properties to enhance structures that may have similar acoustic impedance [9]. Our work points to the extraction of intensity variations observed in RF signals, when subjecting the media under analysis to a temperature change (within the hyperthemia temperature range of 37 to $41°C$. Media temperature variations induce changes in multiple properties such as density and speed of sound (SOS) leading to changes in acoustic attenuation coefficient, echo-shifts and backscattered energy (CBE) [1].

CBE, due to temperature variation, is easy to compute as only the received echo is needed. CBE is primarily dependent on the changes in SOS. Attenuation, density and wave number have shown small influence on CBE within the temperature range considered. Furthermore, experiments have lead to the conclusions that CBE is distinct for different biological scatterers [2] [3]. This fact is particularly interesting as some biological tissues show a predominance in a scatterer type, making CBE potentially proper for non-invasive tissue assessment.

Recent advances in computational power lead to the possibility of simulating real-world physical problems through a computational approach with very good precision. Simulation of ultrasound propagation can be useful in a variety of applications such as to study media properties, transducers and to apply and test multiple signal processing techniques. In this work k-Wave Matlab toolbox was used to simulate CBE in a temperature variated medium [6].

This paper describes, using a K-wave simulation, how CBE tracking has the potential to be the base of future non-invasive tissue assessment methodologies.

2 Methods

2.1 Theoretical model

The predicted change in backscattered energy at temperature T with respect to its value at a reference temperature T_r is given by equation 1, where $\alpha(T)$ is the attenuation and $\eta(T)$ is the backscatter coefficient of the tissue volume, both functions of temperature [4].

$$CBE(T) = \frac{\alpha(T_R)}{\alpha(T)} \frac{\mu(T)}{\mu(T_R)} \frac{1 - e^{-2\alpha(T)x}}{1 - e^{-2\alpha(T_R)x}} \tag{1}$$

Equation 1 can be derived from the single scatterer backscattering coefficient assuming that not only the backscatter coefficient for a distribution of scatterers is proportional to the scattering from a single but also that there is no variation in wave number (<1.5%). Within the temperature range of study, 37 to $41°C$, the attenuation variation is very small and can be negligible, giving raise to equation 2, witch states the primarily dependence of CBE with speed of sound. ρ and C are the density and speed of sound respectively and index letter m and s refer to medium and scatterer properties respectively.

$$\frac{\mu(T)}{\mu(T_R)} = \frac{(\frac{\rho_m C_m(T)^2 - \rho_S C_S(T)^2}{\rho_S C_S(T)^2})^2 + \frac{1}{3}\left(\frac{3\rho_S - 3\rho_m}{2\rho_S - \rho_m}\right)^2}{(\frac{\rho_m C_m(T_R)^2 - \rho_S C_S(T_R)^2}{\rho_S C_S(T_R)^2})^2 + \frac{1}{3}(\frac{3\rho_m - 3\rho_m}{2\rho_S - \rho_m})^2} \tag{2}$$

2.2 Simulation setup

K-wave toolbox [6] is a simulation software designed for time domain acoustic and ultrasound simulations in complex and tissue-realistic media. In its core there is a k-space pseudospectral method (where spatial gradients are calculated using a Fourier allocation scheme, and temporal gradients are calculated using a k-space corrected finite-difference scheme) making its usage not only fast but easy to work with as well [6].

The designed geometry consisted in a 2D medium containing two distinct circular scattering regions, as presented in figure 2.2: one of water-based scatterers (in the left) with a density of 1065 kgm^{-3}, mimicking muscle, and one of lipid-based scatterers (in the right) with a density of 950 $kgm{-}3$, mimicking fat. Scatterers were spread randomly with a density of $64 scatterers/mm^2$ within this circular regions [5][10]. The diameter of each scatterer was $34.7\mu m$ (the size of a single mesh grid element) assuring that the cross section of the scatter is smaller than $2pi\lambda$ and backscattering occurs. Scattering medium of water and lipid based scatters mimic muscle and fat acoustic scattering properties because there is a predominance of these types of scatters in these tissues, respectively.

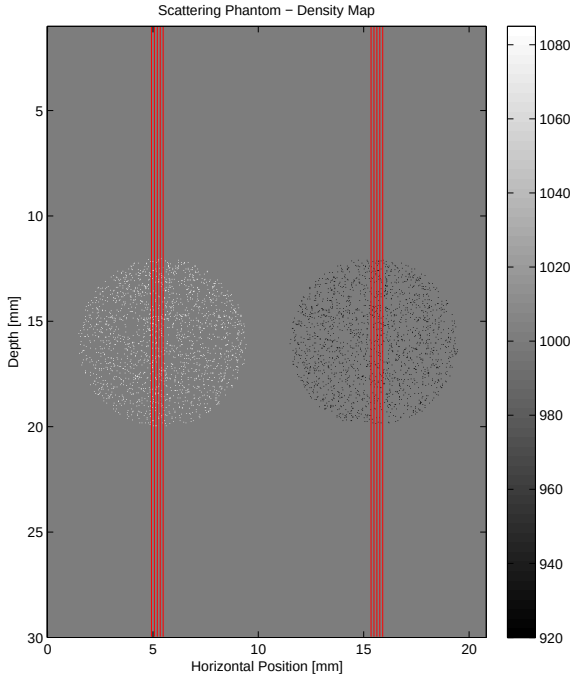

Figure 1: Density map of the simulated phantom - that contains two circular-shaped regions of high scattering content, both with a radius of $4mm$. Water and lipid based scatterers where spread randomly within left and right circular-shaped regions, respectively. The scatterers density in both regions was 64 scatterers$/mm^2$. RF's were extracted from the scan lines depicted by the red lines.

A ultrasound transducer with 128 elements was considered. An excitation pulse with frequency of $7.5MHz$ was established in order to enable a clear comparative view with other studies. RF lines from 5 sites were then acquired for each of the regions as depicted by the red vertical lines on Figure 1. Simulations were repeated with $0.5°C$ intervals from 37 to $41°C$ with the speed-of-sound being variated according to the curves presented in equations 3, 4 and 5 [1].

$$sos_{waterbasedscatterer} = 1571 + 3.9979T - 0.03513T^2 \tag{3}$$

$$sos_{lipidbasedscatterer} = 1810.7 - 13.892T + 0.10160T^2 \tag{4}$$

$$sos_{water} = 3.287156e^{-4}T^3 + -5.779136e^{-2}T^2 + 5.038813T + 1.402385e^3 \tag{5}$$

RF's signals were processed following a conventional approach. The energy of RF envelopes was computed using a square sum as depicted in equation (6). The simulations were repeated using scatterers with a density of 1085 kgm^{-3} for muscle region and 920 kgm^{-3} for fat region.

$$BackscatteredEnergy = \sum_{i=1}^{n} x(i)^2 \tag{6}$$

3 Results

Five RF signals were obtained for each region, one for each red scan line depicted in Figure 2.2. Due to the use of attenuation in the water medium a time-gain compensation was applied.

A conventional RF signal processing was then followed: the excitation pulse was removed and a 4^{th} order butterworth filter was applied. Signals envelopes were obtained, using Hilbert transform, and a compression logarithmic applied with a ratio of 3. As only a fraction of the signals conveys information of interest, a ROI window was chosen containing the region of scattering in both types of tissues (2).

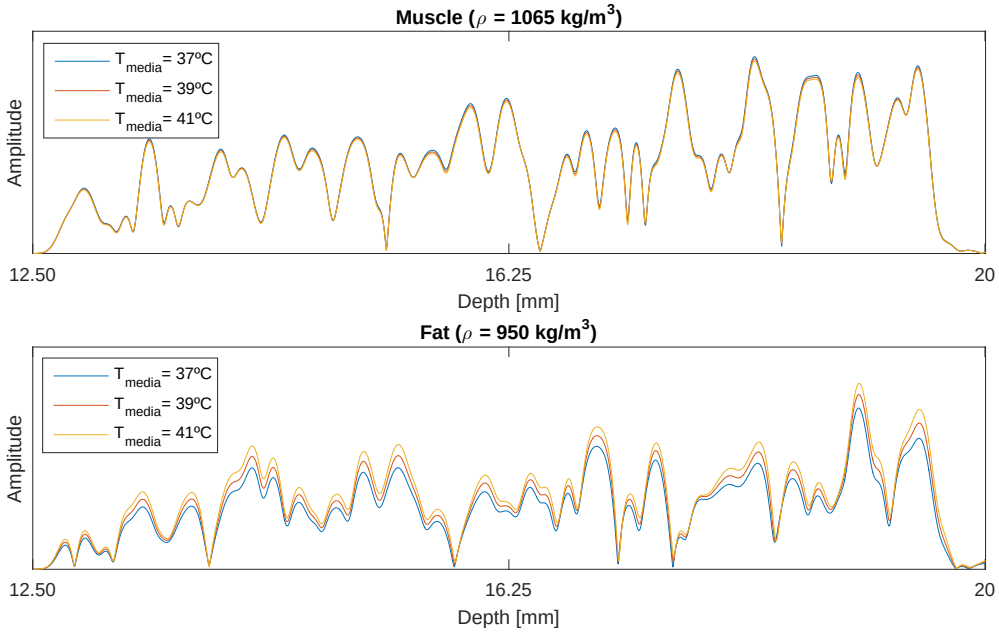

Figure 2: Energy envelopes of the middle RF's scan lines in both regions: muscle with density equals to $1065kg/m^3$ (top plot) and fat with density equals to $950kg/m^3$(bottom plot). A decrease and increase in RF envelope energy can be seen in muscle and fat scattering regions, respectively.

The energy of the RF signals within ROI's were computed for each temperature and plotted along the theoretical CBE for the scatterer type obtained with equations 2, 3, 4, 5. In Figure 3 it is presented the CBE curves obtained with a density of 1065 and 950 kg/m^3 for muscle scatterers and fat scatters respectively. Results of the second simulation in which densities were changed to 1085 kg/m^3 and 920 kg/m^3 for muscle and fat scatters can be visited in Figure 4.

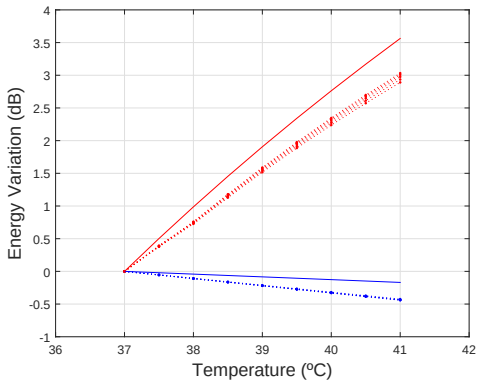

Figure 3: CBE variation with temperature for muscle (red lines) and fat (blue lines) scatterers with density of 1065 and 950 kg/m^3, respectively. The theoretical CBE given by the equation 2 is represented by the continuos lines. The obtained results with simulation are represented by the dashed lines.

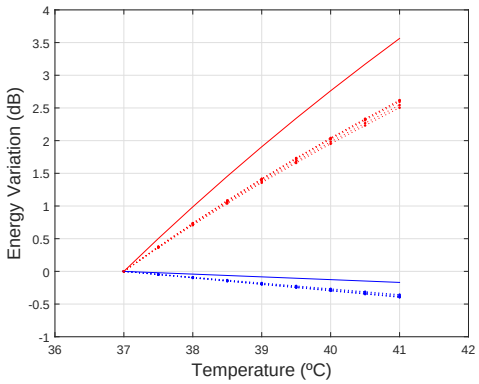

Figure 4: CBE variation with temperature for muscle (red lines) and fat (blue lines) scatterers with density of 1085 and 920 kg/m^3 respectively. The theoretical CBE given by the equation 2 is represented by the continuos lines. The obtained results with simulation are represented by the dashed lines.

Figures 3 and 4 allows us to conclude that simulated CBE curves show a distinct change in backscattered energy in different types of tissues, as it was expected by the theoretical curves plotted in the same figures. In fact, muscle scatterers showed a smooth negative CBE unlike the lipidic ones, that show a clear positive change in backscatter energy.

Table 1: Fit and correlations values obtained with simulated and theoretical data.

	$\rho(kg/m^3)$	Theoretical	Simulated	Corr. Coef.
Muscle	1085	-0.04	-0.09	-0.99
	1065	-0.05	-0.11	-0.99
Fat	950	1.04	0.75	0.99
	920	0.90	0.64	0.99

A linear fit was applied to the mean curve of each tissue (mean of the 5 RF's). Table 1 depicts the fit values obtained for both the theoretical and simulated data, showing that CBE is sensitive to medium changes. Correlation coefficients also shows that there is a positive correlation with temperature for fat and a negative one for muscle.

4 Conclusions

This study has lead to the conclusion that the assessment and classification of tissues non-evasively with a low cost and widely used technique as ultrasound its possible. Future work aims to extend the study to an entire B-Mode image simulation approach as well as the testing in real data.

Acknowledgements

Financial support of the Luso-Brazilian cooperation project CAPES/FCT "Thermo-response".

References

[1] W. L. Straube; R. M. Arthur. Theoretical Estimation of the temperature dependece of backscattered ultrasonic power for noninvasive thermometry. Ultrasound in Med. & Biol., Vol 20 (9), 1994, 915-922.

[2] R. Martin Arthur; W. L. Straube; Jared D. Starman; E. G. Moros. Noninvasive temperature estimation based on the energy of backscattered ultrasound, Medical Physics Vol 30 (6), 2003, pp 1021-1029.

[3] R. M. Arthur, W. L. Straube, J. W. Trobaugh, and E. G. Moros, “Non-invasive estimation of hyperthermia temperatures with ultrasound,” International journal of hyperthermia, Vol 21, 2005, pp. 589–600.

[4] R. Martin Arthur, Jason W. Trobaugh, William L. Straube and Eduardo G. Moros, Temperature Dependence of Ultrasonic Backscattered Energy in Motion-Compensated Images. IEEE, 2016.

[5] Po-Hsiang Tsui, Ultrasound Detection of Scatterer Concentration by Weighted Entropy. Entropy Vol 17, 2015, pp. 6598-6616.

[6] Bradley E. Treeby, Jiri Jaros, Alistair P. Rendell and B. T. Cox , Modeling nonlinear ultrasound propagation in heterogeneous media with power law absorption using a k-space pseudospectral method, Acoustical Society of America Vol 131, 2012, pp 4324–4336.

[7] E. M. Haacke, W. R. Brown, R. M. Thompson, and R. Venkatesan, Magnetic Resonance Imaging: Physical Principles and Sequence Design. Wiley-Liss, 1999.

[8] W. R. Hedrick, L. D. Hykes, and L. D. Starchman, Ultrasound Physics and Instrumentation. Mosby, 1992, pp. 153–156.

[9] J. Ophir, I. CCspedes, H. Ponnekanti, Y. Yazdi and X. Li , Elastography: A Quantitative Method for Imaging the Elasticity of Biological Tissues, Ultrasound Imaging, Vol 13, 1991, pp. 111-134

[10] Medical ultrasound parameters ultrasound. [Online (2016, May)]. Available: http://www.imi.ncku.edu.tw/modules/content/talks/971121Image.pdf

ICA 2016 BUENOS AIRES
Buenos Aires – 5 to 9 September 2016
Acoustics for the 21st Century...

PROCEEDINGS of the 22nd International Congress on Acoustics

Ultrasound: Paper ICA2016-348

A complete COMSOL and MATLAB finite element medical ultrasound imaging simulation

R. J. Simões[(a)], A. Pedrosa[(a)], W. C. A. Pereira[(b)] and C. A. Teixeira[(a)]

[(a)]Centre for Informatics and Systems, Polo II, University of Coimbra, Portugal, ricardodiassimoes@gmail.com
[(b)]Biomedical Engineering Program-COPPE, Federal University of Rio de Janeiro, Brazil, wagner.coelho@ufrj.br

Abstract

Ultrasound imaging is widely used in medical diagnosis. The urge of new methodologies that upgrade the ultrasound imaging quality are essential to improve the medical diagnosis. A straightforward and low-cost way to assess ultrasound imaging capabilities is by the development of accurate simulations. Here, with this simulation, we aim to establish a base for realistic and more detailed simulations leading to a fast and reliable evaluation of different array parametrization and wave propagation.The simulation was developed using real scenario properties to improve results reliability. Wave-propagation is analyzed from the 100 millimeter AIUM test object. The results suggest agreements with literature. Metrics like signal-to-noise ratio and image entropy trend in same way as in real scenarios. To the best of our knowledge, this is a simulated reliable complete medical ultrasound imaging system using a finite element approach.

Keywords: Simulation, Finite Element Methods, Medical Ultrasound

1 Introduction

Ultrasound (US) can be defined as acoustic waves with higher frequencies than human can hear. For medical purposes like imaging and therapeutic physiotherapy, this frequency range goes from 1MHz to 50MHz [10]. A trade-off between resolution and penetrating ability exists i.e, better resolutions are achieved using higher frequencies and better penetration is obtained using low frequencies [10].

The US acoustic waves are generated using materials with piezoelectric properties, i.e., using a conversion between mechanical energy and electrical energy. Therefore, an electric radiofrequency (RF) signal is converted into a pressure wave that propagates through a medium [3]. In the medium, the generated wave is reflected, scattered, diffracted, refracted and absorbed, and thus, by these interactions, the pressure acoustics wave is attenuated. The portion which is reflected and scattered back to the transducer is used to generate ultrasound images that are widely used in current medicine to see different types of organ structures and to measure blood flows within the circulatory system.

After echoes are received by the transducer and converted to electrical signals, it is necessary to do a beamforming to increase the signal-to-noise ratio (SNR). A correct beamforming process must follow the Nyquist requirement, this way, a high temporal resolution is achieved, avoiding deterioration of the signal [9]. Normally, the beamforming process begins with a transducer apodization to avoid the influence of side lobes and undesired reflections leading to image artifacts. Apodization decreases the signal excitation from the edge piezoelectric elements by using windows [9].

Filtering in the frequency domain improves the SNR from the received raw signal [5]. Low-pass filters like Butterworth, Chebyshev, among others, suppress undesired frequencies, however with the frequency elimination some information from the raw signal could be lost, thus, it is necessary a compromise between erased frequencies and lost information [5].

Envelope detection is made to quantify the reflection energy associated to the signal. This energy is then processed to enhance details by logarithmically compressing the resulting signal envelope. Nevertheless, in US medical imaging, usually, the energy from the reflections are low due to similarities between medium acoustic impedances. To minimize this problem, an adequate processing approach should be made to improve the quality of the envelope and to extract the maximum information.

In this work, we design and implement (in a Finite Element Analysis (FEA) environment) a time domain simulation that reproduces the coupling between a transducer array and an AIUM 100mm test object used to evaluate the axial resolution. In this simulation, the wave-propagation with different apodization approaches and the data acquired from the medium reflections are analyzed. In the beamforming, we apply processing methods like filtering techniques and its effect in the SNR. Also, envelope techniques are evaluated with the entropy metric. Then, the results are qualitatively compared with literature [9] and main conclusions are extracted.

Our goal is to establish a simulation model for future probe designs and image simulation that

will help on the understanding of different phenomena involved. This is a complete medical ultrasound wave propagation where the consequent image formation is done. Until now, few probes were designed in a FEM environment. One example is the the one described by [17] where there is no simulated a wave propagation in time domain or image formation. Also, the main ultrasound wave propagation simulations are reproduced in a finite-difference time-domain (FDTD) [16, 2, 15]. However there are some ultrasound FEM simulations like [1, 6, 8] but few for a complete medical ultrasound image formation like the one developed here.

2 METHODOLOGY

2.1 256-Element Array Transducer Design and Simulation Properties

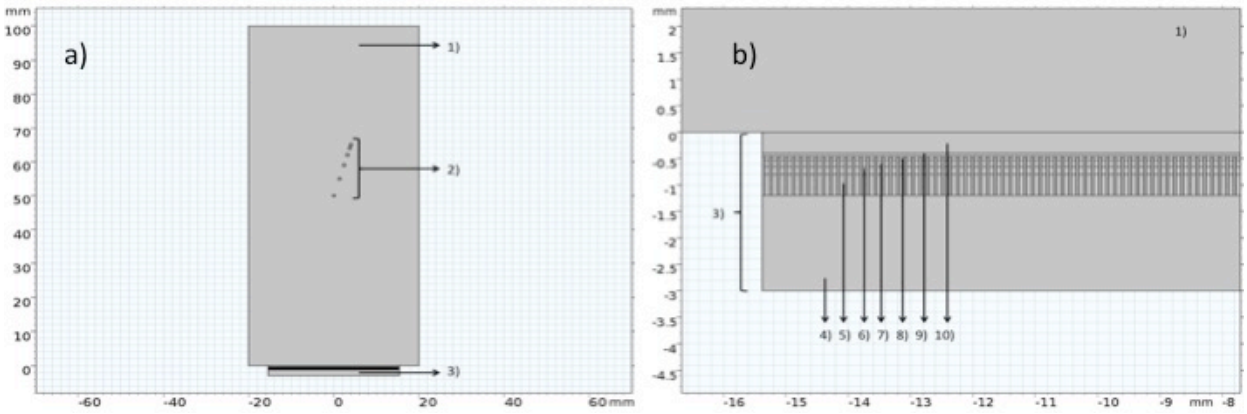

Figure 1: Simulation geometry where 1) is water, 2) are stainless steel rods, 3) is the simulated transducer and the numbers 4) to 10) represent the backing, matching Layer 1 (ML1), matching Layer 2 (ML2),matching Layer 3 (ML3),matching Layer 4 (ML4) and lens, respectively. (a) is the entire geometry and b) is a zoom from the transducer geometry).

The 256-element array transducer with 0.12mm of pitch surrounded by materials structures with particular acoustical properties is designed to produce punctual wave fronts that have the same phase to enable constructive overlap, and thus, generate a unique front wave. There are several aspects that one should take into account when designing a transducer: it is necessary to know all the acoustical material properties; the multiple vibration modes of the array elements like shear modes from cross-talking; the array dimension should be generally limited with a pitch width in a range $[< \frac{\lambda}{2}; \frac{3\lambda}{2}]$, where λ is the wavelength. When the pitch width is $\lambda/2$ the transducer is called fully sampled [13].

In Figures 1a) and 1b) the used geometry can be seen where all the geometry domain is seen and the the zoom to the probe site, respectively.

Table 1: Backing Material properties used in simulation material properties.

Properties	Value
Young's Modulus (E)	$71 \times 10^9 Pa$
Density (ρ)	$7750(kg/m^3)$
Poisson's Ratio	0.46
Rayleigh damping factor α	$8 \times 10^6 (s^{-1})$
Rayleigh damping factor β	$1.5 \times 10^{-9}(s)$

Table 2: Matching Layer Properties

	ML1	ML2	ML3	ML4	Lens	Filler
Length (mm)	0.15	0.11	0.08	0.06	0.4	-
Density (kg/m3)	8000	3500	1100	1100	1100	1000
Poisson's Ratio	0.42	0.44	0.45	0.45	-	0.485
Young's Mod(GPa)	10	4.4	2	0.9	-	0.35
SOS (m/s)	-	-	-	-	1060	-

2.2 Wave Propagation Simulation

The medium simulation mimics a structure present in the AIUM 10mm test object used to assess the axial resolution [7]. The AIUM object is composed by a box filled with distilled water where stainless steel rods are placed in specific sites. Table 1, Table 2 and Table 3 present the backing, matching Layer and medium properties, respectively.

The geometry used is a 2D representation of a transducer coupled to a medium. The 2D representation decreases the computational time and shows similar results as 3D computation slices [1]. Also, the wave propagation was modeled as linear wave equation for simplicity.

An electrical potential must be given to the transducer terminals to obtain the desired mechanical displacement. The potential given to the terminals is modeled by equation 1:

$$V = V_0 sin(\omega t + t_0) \tag{1}$$

where V is a potential difference in Volts and $V_0 = 150(V)$ is the maximum potential,. $\omega = 2\pi f$, with $f = 1MHz$ and t_0 is an optional phase given to the terminals. This way, a sine wave is produced with a desired fundamental frequency, f [14] which in our case is 1MHz. This frequency value also enables simulation in an acceptable computation time. A frequency of 1MHz in water has a consequent wavelength of 1.54mm. The modeled sine burst has three complete periods and a resulting length of 4.62mm. Usually, in FEA of wave propagation, the mesh length must be within the range of [λ/5; λ/10] [1, 17].

The wave dynamic is defined by equation 2 [4].

$$\frac{1}{\rho c^2}\frac{\partial^2 p_t}{\partial t^2} - \frac{1}{\rho}(\nabla_{p_t} - q_d) = Q_m \tag{2}$$

where $\rho(kg/m^3)$ is the medium density, $c(m/s)$ is the medium speed of sound, $p_t(Pa)$ is the

Table 3: Medium properties

	Water	Steel Rods
Density (kg/m^3)	1000	7500
Speed of Sound (m/s)	1481.4	5790

acoustic pressure, $q_d(N/m^3)$ and $Q_m(1/s^2)$ is the dipole source and source monopole, respectively. Both of the source terms are optional and the default value is zero.

2.3 Signal Beamforming

Raw ultrasonic signals are generated from the COMSOL® Multyphysics simulation and, then, processed with Matlab® (The mathworks). The received pressure signals at each active transducer element are processed into a single A-Line scan. As we simulate a 256-element transducer, 256 A-Mode scanlines were used to generate the B-mode image. The beamforming weights are automatically computed based on the defined transducer focus distance and on the RF signal normalization. After beamforming, the first part of each scan line originated by the excitation pulse is removed. This step is required because probes allow the signal acquisition of sending and receiving pressures at the same time.

The region of interest (ROI) is only a segment reflected from the AIUM test object which in this work is the area where the steel rods are positioned. Each element that compose the ROI matrix corresponds to a distance from the transducer (ΔL), computed as: $\Delta L = ct/2$, where c is the medium speed of sound (SOS) and t is the time-of-flight (TOF) of the wave.

Apodization is the amplitude weighting of normal velocity across the aperture, one of the main reasons for apodization is to lower the side lobes on either side of the main beam to decrease noise from undesired side reflections. Aperture function needed to have rounded edges that taper toward zero at the limits of the aperture to create low side lobes levels [12, 9]. We used a Rectangular window (same as no window [9]) and a Hamming window. Then, the envelope detection is made by appling an Hilbert transform.

The variation in the amplitude of the RF data is relatively high, i.e., the presence of a few very high amplitude points in the image overshadows everything else. In order to achieve a balance, the amplitude values are mapped nonlinearly by a logarithmic-looking function which adjusts the dynamic range [11]. Here, our images suffer a 50dB log compression.

3 RESULTS

3.1 Piezoelectric Effect and Wave Propagation Simulation

Rectangular and Hamming window displacements are represented in Figures 2a), 2b) respectively. Looking at the images it is possible observe the different displacements that are consequence from the potential windows at the transducer terminals.

The resulting wave propagations can be seen for the the rectangular and Hamming window

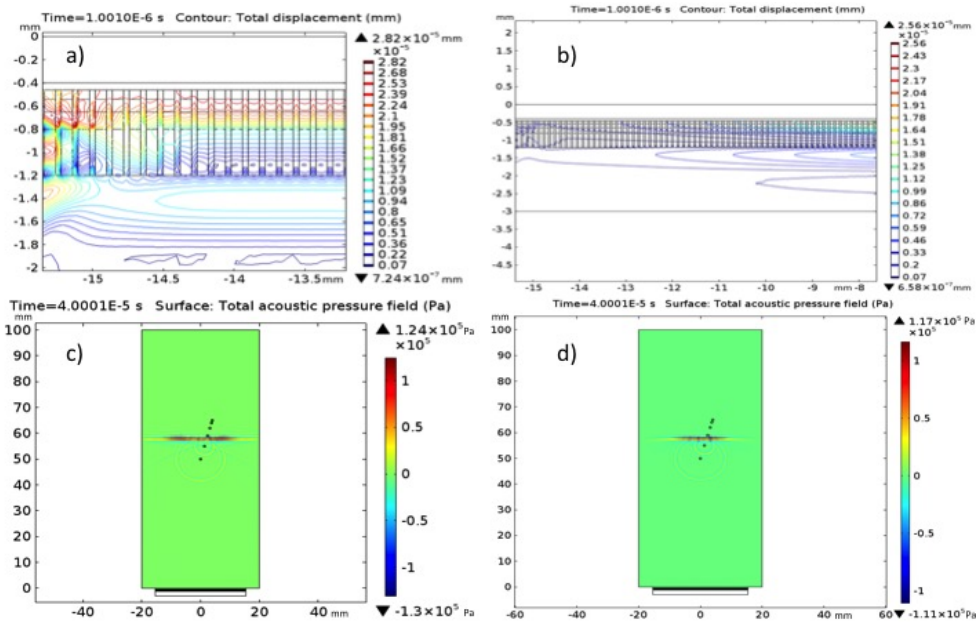

Figure 2: Transducer border displacement for a) Rectangular window, b) Hamming window in both images it is possible to observe the displacement contours made by the transducer at 1e-6s. Wave propagation in a water medium with reflection in steel rods at t=4.0005e-5s for c) Rectangular window, d) Hamming Window

apodization in Figures 2c) and 2d) at t=4.0005e-5s, respectively. Also, it is possible to see a reflection from the steel rods.

3.2 Signal Processing

From the simulation signals it is possible to perform signal processing. In the Table 4 the SNR related is presented to a simple signal processing which apodization and filtering are made. Chebyshev filters are added to each apodization to infer the best window-filter pair. In Figure 3 it is represented the SNR values for visualization.

After the SNR analysis, all the signals are submitted to envelope detection and the results are represented in Table 4 where the Entropy of each simulated US image is analyzed. In Fig-

Table 4: SNR from three window types: rectangular and Hamming with different signal filters approaches: Raw, Butterworth, Chebyshev (Type1).

Apodization Window	Filter	Mean SNR (dB)	Entropy
Rectangular	Raw	6.5813	5.758
Rectangular	Chebyshev	10.7440	3.462
Hamming	Raw	25.8007	5.567
Hamming	Chebyshev	27.1278	3.385

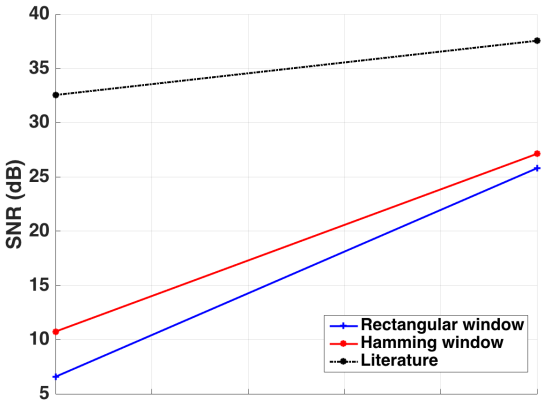

Figure 3: SNR graph from the worst Filter approach for all windows VS the best Filter approach for all windows and the similar approaches from literature [9] for the rectangular and hamming windows.

ure 4a) and 4b), there are plotted all the approaches for a single RF signal, where is possible to visually compare the different methodologies of the signal processing. In Discussion we analyze the obtained results.

Finally, the envelope detection is applied to all RF signals and a image is generated with a log compression of 50dB. In Figures 5a), 5b), 5c) and 5d), the final US simulated images can be seen.

4 DISCUSSION

In this simulation we design a 256-element PZT-5A transducer which is excited with a sinusoid with 200V at the terminals. This voltage generates mechanical energy that is transmitted to the medium. The excitation of the transducer is tested using two types of window apodization. A rectangular an Hamming window is added to the terminals to verify the improvement of SNR which is also verified in [9]. Observing Figure 2a), we can see the window effect on the piezoceramic displacement where the displacement of the ceramics is more evident in the transducer side than in Figure 2b) where an Hamming window is applied and the displacement is almost inexistent.

The different window approaches generate different propagations in the medium. Between Figures 2c) and 2d) it is possible to observe notorious differences in the pulse width.

After the acquisition of the RF signals, they were pre-processed with a Chebyshev (type1) filter. All the signals are quantified in Table 4 where the SNR is evaluated for each method. As referenced in literature [9], the worst case scenario is for the rectangular window without filter where the SNR is the lowest comparing to the Hamming window where the SNR is slightly improved. In the Table 4 we, also, infer the same facts. The worst SNR is for pair rectangular

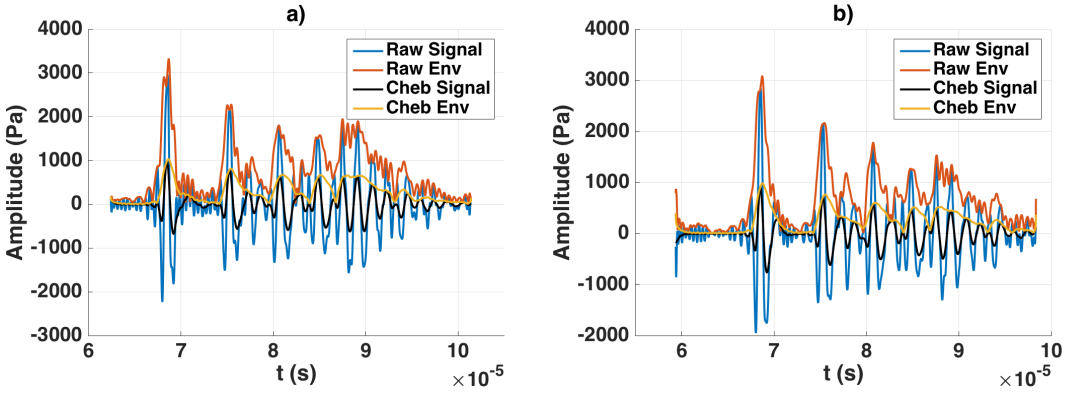

Figure 4: A RF signal from the right middle piezoceramic, where it is possible see all the different envelope detection approaches for a) Rectangular Window, b) Hamming window.

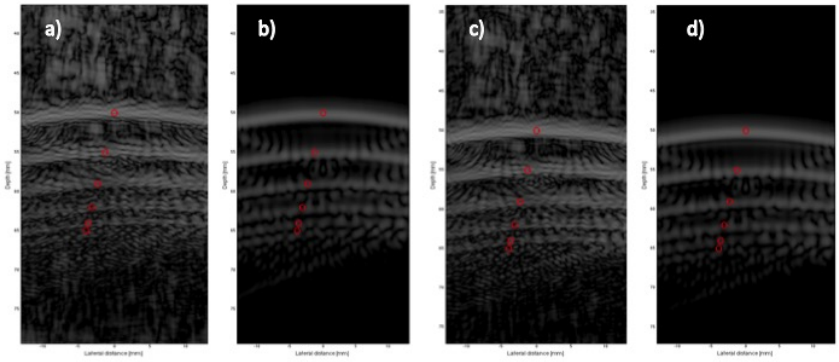

Figure 5: Simulated US images from an Hilbert analytical signal envelope detection method for a) Rectangular window, b) Chebyshev filter with a Rectangular window, c) Hamming window and d) Chebyshev filter with a Hamming window.

window with a raw signal where the SNR value is 6.5813(dB). However this value is improved when the Chebyshev filter is applied. The best SNR value is for the Hamming window with a Chebyshev filter which is 27.1278(dB). The Hamming window results are notoriously improved compared with the rectangular window for all the width and without filter processing. In fact, the difference between Rectangular and Hamming are evident and that fact is observed in the SNR quantification. From the filter point of view, the Chebyshev filter improves the signal for both windows applied. In Figure 3, it is visually illustrated the SNR differences, where it is observable the SNR improvement for the two different windows.

In Table 4 is represented the entropy for each window-filter pair. The entropy is measured

after the envelopes suffer a log compression of 50dB to improve the image texture allowing the extraction of details. Analyzing Table 4, it is possible to see that SNR values are consistent with the entropy values for all the different approaches of signal processing. Nevertheless, the most noisy image is the Raw Signal with a rectangular window where the entropy value is maximum, 5.758. The similarity of entropy between the raw signals can be observed in Figures 5a) and Figure 5c) where, the images are noisy compared to the other two Figures (5b) and 5d)), where the images are less noisy. Consequently the value of entropy for the best case scenario is 3.385 where an Hamming window and a Chebyshev filter is used. Another fact that emphasizes the ideal character of the simulation is the continuous line that detects the rod, i.e, there is no loss of energy and the wave is detected in all the piezoceramics.

Finally, the results either SNR or image entropy follows the literature data, in generally.

5 CONCLUSION

This work is a basis for future more advanced simulations. The results allow us to believe the rightness about the simulation methodology due to its accordance with the literature.

The use of FEM simulation allows the control all the physical variables like the piezoceramics material, medium temperatures, among other variables, property that does not exist in most of US simulators so far developed, so the implementation of this kind of simulation is extremely useful to predict real case scenarios.

For future work, in a short-term and mid-term, we will develop a complete phased-array probe simulation with the respective US image processing and develop a physical probe to compare quantitative the resulting signals and images.

ACKNOWLEDGMENT

Financial support of the Luso-Brazilian cooperation project CAPES/FCT "Thermo-response".

References

[1] D. Andrews. Modelling of ultrasonic transducers and ultrasonic wave propagation for commercial applications using finite elements with experimental visualization of waves for validation. *Proceedings of the 2014 COMSOL*, 2014.

[2] E. Bossy, F. Padilla, F. Peyrin, and P. Laugier. Three-dimensional simulation of ultrasound propagation through trabecular bone structures measured by synchrotron microtomography. *Physics in medicine and biology*, 50(23):5545, 2005.

[3] J. D. N. Cheeke. *Fundamentals and applications of ultrasonic waves*. CRC press, 2010.

[4] I. COMSOL Multiphysics. *Introduction to Acoustics Module*. COMSOL, 2015.

[5] A. Dourado. Lecture notes in algoritmos de diagnostico e auto-regulacao, October 2013.

[6] M. B. Drozdz. *Efficient finite element modelling of ultrasound waves in elastic media*. PhD thesis, Imperial College London, 2008.

[7] K. Erikson, P. Carson, and H. Stewart. Field evaluation of the aium standard 100 mm test object. In *Ultrasound in Medicine*, pages 445–451. Springer, 1976.

[8] O. Goksel and S. E. Salcudean. B-mode ultrasound image simulation in deformable 3-d medium. *Medical Imaging, IEEE Transactions on*, 28(11):1657–1669, 2009.

[9] M. A. Hassan and Y. M. Kadah. Digital signal processing methodologies for conventional digital medical ultrasound imaging system. *American Journal of Biomedical Engineering*, 3(1):14–30, 2013.

[10] W. R. Hendrick. *Ultrasound Physics and Instrumentation*. Mosby, 1995.

[11] J. A. Jensen. Users' guide for the field ii program. *Technical University of Denmark*, 2800, 2001.

[12] O. Kripfgans. Ultrasonic imaging. *Encyclopedia of Medical Devices and Instrumentation*, 2006.

[13] E. Lacaze, S. Michau, and P. Mauchamp. 20 mhz ultrasound array for medical imaging from design to image evaluation. In *Ultrasonics Symposium, 2001 IEEE*, volume 2, pages 1139–1142. IEEE, 2001.

[14] R. Lerch. Simulation of piezoelectric devices by two-and three-dimensional finite elements. *Ultrasonics, Ferroelectrics, and Frequency Control, IEEE Transactions on*, 37(3):233–247, 1990.

[15] M. Liebler, S. Ginter, T. Dreyer, and R. E. Riedlinger. Full wave modeling of therapeutic ultrasound: Efficient time-domain implementation of the frequency power-law attenuation. *The Journal of the Acoustical Society of America*, 116(5):2742–2750, 2004.

[16] G. Pinton, J.-F. Aubry, M. Fink, and M. Tanter. Effects of nonlinear ultrasound propagation on high intensity brain therapy. *Medical physics*, 38(3):1207–1216, 2011.

[17] L. Spicci. Fem simulation for 'pulse-echo'performances of an ultrasound imaging linear probe. *Proceedings of the 2012 COMSOL*, 2012.